

AD\_\_\_\_\_

Award Number: W81XWH-05-1-0396

TITLE: Angiogenic Signaling in Living Breast Tumor Models

PRINCIPAL INVESTIGATOR: Edward Brown, M.D.

CONTRACTING ORGANIZATION: University of Rochester  
Rochester, NY 14627-0140

REPORT DATE: June 2008

TYPE OF REPORT: Annual

PREPARED FOR: U.S. Army Medical Research and Materiel Command  
Fort Detrick, Maryland 21702-5012

DISTRIBUTION STATEMENT: Approved for Public Release;  
Distribution Unlimited

The views, opinions and/or findings contained in this report are those of the author(s) and should not be construed as an official Department of the Army position, policy or decision unless so designated by other documentation.

REPORT DOCUMENTATION PAGE				Form Approved OMB No. 0704-0188	
Public reporting burden for this collection of information is estimated to average 1 hour per response, including the time for reviewing instructions, searching existing data sources, gathering and maintaining the data needed, and completing and reviewing this collection of information. Send comments regarding this burden estimate or any other aspect of this collection of information, including suggestions for reducing this burden to Department of Defense, Washington Headquarters Services, Directorate for Information Operations and Reports (0704-0188), 1215 Jefferson Davis Highway, Suite 1204, Arlington, VA 22202-4302. Respondents should be aware that notwithstanding any other provision of law, no person shall be subject to any penalty for failing to comply with a collection of information if it does not display a currently valid OMB control number. <b>PLEASE DO NOT RETURN YOUR FORM TO THE ABOVE ADDRESS.</b>					
1. REPORT DATE (DD-MM-YYYY) 01-06-2008		2. REPORT TYPE Annual		3. DATES COVERED (From - To) 1 Jun 2007 – 31 May 2008	
4. TITLE AND SUBTITLE  Angiogenic Signaling in Living Breast Tumor Models				5a. CONTRACT NUMBER	
				5b. GRANT NUMBER W81XWH-05-1-0396	
				5c. PROGRAM ELEMENT NUMBER	
6. AUTHOR(S)  Edward Brown, M.D.  E-Mail: <a href="mailto:edward_brown@urmc.rochester.edu">edward_brown@urmc.rochester.edu</a>				5d. PROJECT NUMBER	
				5e. TASK NUMBER	
				5f. WORK UNIT NUMBER	
7. PERFORMING ORGANIZATION NAME(S) AND ADDRESS(ES)  University of Rochester Rochester, NY 14627-0140				8. PERFORMING ORGANIZATION REPORT NUMBER	
9. SPONSORING / MONITORING AGENCY NAME(S) AND ADDRESS(ES) U.S. Army Medical Research and Materiel Command Fort Detrick, Maryland 21702-5012				10. SPONSOR/MONITOR'S ACRONYM(S)	
				11. SPONSOR/MONITOR'S REPORT NUMBER(S)	
12. DISTRIBUTION / AVAILABILITY STATEMENT Approved for Public Release; Distribution Unlimited					
13. SUPPLEMENTARY NOTES					
14. ABSTRACT In this grant we propose to elucidate the signaling pathway that translates VEGFR activation into elevated vessel permeability, in endothelial cells within living breast tumor models. The working hypothesis is that the signaling pathway involved is a constitutively active form of the pathway shown for healthy mesenteric microvessels. Progress to date includes the training of personnel in the laboratory, the completion of instrumentation development for a novel method for the measurement of convective flow in tumors in vivo and extensive analysis of its capabilities, extensive investigation of breast tumor extracellular matrix using second harmonic generation, extensive analysis of the abilities of a novel permeability measurement technique and numerous preliminary experiments to establish methodology for tasks to commence in upcoming years.					
15. SUBJECT TERMS Angiogenesis, microscopy, signaling, VEGF, permeability					
16. SECURITY CLASSIFICATION OF:			17. LIMITATION OF ABSTRACT	18. NUMBER OF PAGES	19a. NAME OF RESPONSIBLE PERSON
a. REPORT	b. ABSTRACT	c. THIS PAGE			USAMRMC
U	U	U	UU	64	19b. TELEPHONE NUMBER (include area code)

## Table of Contents

<b>Introduction.....</b>	<b>4</b>
<b>Body.....</b>	<b>4</b>
<b>Key Research Accomplishments.....</b>	<b>22</b>
<b>Reportable Outcomes.....</b>	<b>22</b>
<b>Conclusions.....</b>	<b>23</b>
<b>References.....</b>	<b>N/A</b>
<b>Appendices.....</b>	<b>24</b>

## **Introduction.**

Current anti-angiogenic therapies focus on the earliest steps in the angiogenic signaling cascades and try to prevent angiogenic molecules (i.e. VEGF, Ang-1, TGF- $\alpha$ ) from reaching endothelial cells or try to prevent activation of their endothelial cell (EC) receptors. However, the study of downstream steps, within tumor ECs, as an avenue for treatment has been neglected. Furthermore, due to a lack of appropriate *in vivo* imaging and measurement tools, these EC signaling cascades have been explored almost exclusively in thin preparations of healthy vessels (i.e. vessels in the easily accessible, 25 micron mesenteric membrane) or in endothelial cells in a dish, and the signaling machinery that is delineated varies depending upon which type of healthy vessel provides the ECs. As tumor vessels are fundamentally unlike any of the healthy vessels in the body, we don't know which of the known signaling pathways are involved in *in vivo* tumor angiogenesis, *or if any of them are*. Consequently, we propose to elucidate the signaling pathway that translates VEGFR activation into elevated vessel permeability, in endothelial cells within living breast tumor models. The working hypothesis is that the signaling pathway involved is a constitutively active form of the pathway shown for healthy mesenteric microvessels. We have identified several signaling molecules that we hypothesize will play key roles in that pathway. In each case we will pharmacologically enhance or inhibit the action of a given molecule, and use advanced *in vivo* imaging techniques that we are currently developing or have previously developed to probe the resultant alterations in the VEGF/permeability relationship, with EC internal calcium dynamics as a key intermediate readout. Elucidation of this pathway is motivated by the desire to find new therapeutic targets, with which to block tumor angiogenesis and hence restrict tumor growth. Current angiogenic therapies, which favor blocking transit of an angiogenic factor to the ECs or inhibition of receptor activation, often fail because there can be several parallel pathways for angiogenic signals to travel from tumor cells to ECs, and when one is blocked, others are utilized. Signaling that occurs downstream of endothelial receptor activation may provide a signaling 'bottleneck' that several angiogenic factors utilize in common and hence may provide a uniquely powerful therapeutic target which circumvents the development of drug resistance.

## **Body**

We are now concluding the third year of this grant, as well as the third year of my laboratory, here in the Department of Biomedical Engineering at the University of Rochester Medical Center. My laboratory now consists of myself, Kelley Madden, a Research Assistant Professor in BME, Khawarl Liverpool, a technician, and five graduate students, of which Ryan Burke and Javier Lapeira in BME, as well as Kelley Sullivan in Physics are currently funded by this grant. What follows is a discussion of our progress in each of the Tasks in our original Statement of Work, starting with those tasks that were scheduled to begin earliest, and finishing with later tasks.

## **Progress on Task 7**

Chronologically, the earliest goals in my statement of work are Tasks 7 and 9. In its entirety, Task 7 is:

**Task 7.** Determine the relative contribution of convection versus diffusion in transport of fluorescent tracer out of a tumor vessel. (Years 1 and 2)

- A.** Develop theory and perform in vitro tests of the ability of Multiphoton Fluorescence Recovery After Photobleaching to simultaneously measure diffusion and convection.
- B.** Determine relative contribution of convection versus diffusion in transport out of a tumor vessel during steady state conditions.
- C.** Determine relative contribution of convection versus diffusion in transport out of a tumor vessel after acute alteration in tumor vessel permeability.

At the end of year two we had the MP-FRAP equipment fully functioning, as well as largely automated via LabVIEW and MATLAB for increased throughput of data taking and analysis. Development of the theory (task 7a) required not only mathematical derivation of a new recovery model, but also testing of the model via computer simulations to determine the relevant range of diffusion and velocity that can be accurately measured based on the computational constraints of the three component fit required by the new model. To this end, we wrote several programs in MATLAB to generate data using the new flow model and to fit the data using either the standard no-flow model or the new flow model. At the end of year two, we had successfully evaluated the limitations of the standard, no-flow MP-FRAP model to correctly fit fluorescence recovery curves with a flow component. We did this by generating simulated data using the flow model, fitting it to the standard model, then calculating ratios of fit diffusion coefficient to input diffusion coefficient. Any ratio different from one would indicate a poor fit. Early in year three, we also completed evaluation of the ability of the flow model to fit fluorescence recovery curves with convective flow. This was accomplished by generating data using the flow model, fitting with the flow model, and then calculating ratios of fit diffusion coefficient to input diffusion coefficient and of fit to input velocity.

Early in year three we produced a simple experimental apparatus to generate solutions with known flow velocities and known diffusion coefficients. We then performed MPFRAP and used the standard and flow models to fit the resultant curves, evaluating the capabilities of the two models. In Figure 1, we compare the ability of the standard and flow models to accurately determine the diffusion coefficient over this range of velocities. On the horizontal axis, we introduce a scaled velocity such that  $v_s = \text{velocity} \cdot (w_r/8D)$ , where  $w_r$  is the radial dimension of the two-photon focal volume. Our previous simulations have shown that this scaled velocity is the relevant parameter in describing any combination of flow and diffusion in MPFRAP. This allows us to define universal “cutoff velocities” for both the standard and flow models, beyond which the particular model fails to yield accurate diffusion coefficients and/or velocities.

Figure 1. A series of experimental recovery curves for FITC-BSA and FITC-2000kD dextran taken over a wide range of known flow velocities. The curves were then fit to both the standard MP-FRAP model and the flow MP-FRAP model, and the diffusion coefficient produced by the fit was normalized to the known value measured in the absence of flow. Hence, an accurate result produces a ratio of one. As the scaled flow velocity grows beyond  $v_s \sim 0.3$ , the standard MP-FRAP model yields an overestimate to  $D$ . The flow model, however, continues to provide accurate  $D$ s for scaled velocities approximately 10x higher.

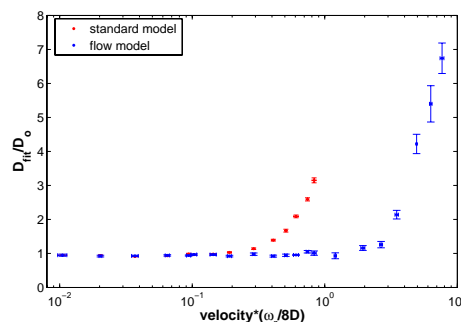
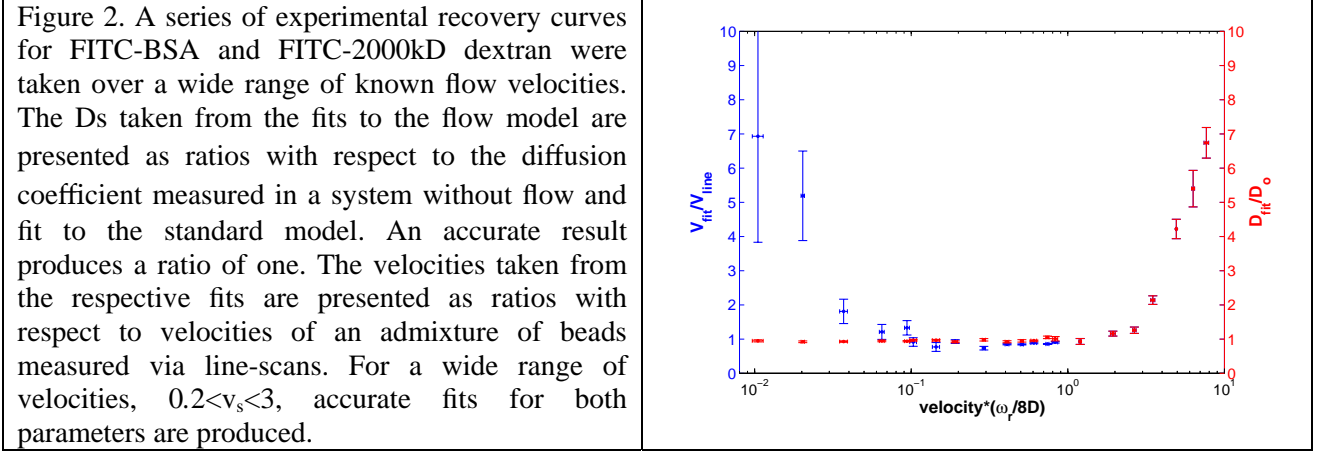


Figure 2 displays the accuracy of both the diffusion coefficient and the velocity as determined by the flow model. From this data we can define three regimes for the flow model: 1. diffusion-dominated, in which only the diffusion coefficient is accurately determined, 2. balanced, in which the diffusion coefficient and velocity are both accurately determined, and 3. velocity-dominated, in which only velocity is accurately determined. Again, by scaling the velocity along the horizontal axis, we collapse the curves for each diffusion coefficient onto a single curve and can define universal scaled velocity values for the transition between each regime. For this bleach depth parameter ( $\beta=0.6$ ) and noise (3%) the cutoff velocities are 0.2 for the transition from diffusion dominated to balanced, and 3.0 for the transition from balanced to velocity dominated. The scaled velocity defining the transitions between the regimes compare well with the values determined by the simulations.



We also demonstrated the effectiveness of the technique *in vivo* by measuring diffusion and velocity *within* tumor vessels of 4T1 murine mammary adenocarcinomas implanted in the dorsal skinfold chamber. By continuing to employ the line-scan technique, we concurrently measured the red blood cell (RBC) velocity, which was used as an independent *in vivo* measurement of transverse flow to compare with our MP-FRAP velocity measurements. Table 1 tabulates the results from three vessels, chosen for their position in the diffusion dominated, balanced, and velocity dominated regimes. In each case our predictions of accuracy based upon calculation of  $v_s$  from the RBC velocity and known  $D$  exactly matched the behavior of the MPFRAP fit.

Table 1 Results of fitting experimental *in vivo* data of diffusion and convection in tumor vessels using both the standard and flow models.

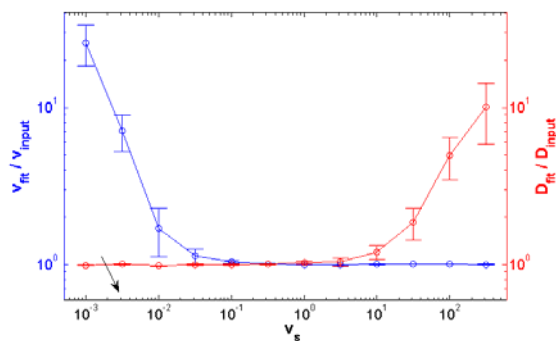
	$v_s$	$D_{\text{standard}} (\mu\text{m}^2/\text{s})$	$D_{\text{flow}} (\mu\text{m}^2/\text{s})$	$v_{\text{flow}} (\mu\text{m}/\text{s})$	$v_{\text{RBC}} (\mu\text{m}/\text{s})$
vessel 1	$0.08 \pm 0.02$	9.28	9.28	0.02	$14 \pm 3$
vessel 2	$0.45 \pm 0.05$	19.6	9.68	69.3	$83 \pm 10$
vessel 3	$6.24 \pm 0.44$	250	34.9	987	$1139 \pm 80$

We have recently submitted a manuscript on this improvement to the MPFRAP technique to the Biophysical Journal, and have attached the manuscript to this progress report. I feel it has a high

likelihood of publication, and will be a significant advance in the field. MPFRAP will now be able to be performed in the presence of unknown flows, and the diffusion coefficient and velocity accurately determined. Importantly, our manuscript demonstrates how to perform a “sanity check” calculation using the *output* parameters of a fit, with no *a priori* knowledge of the ground truth, to determine if the parameters are accurate, or were rendered inaccurate by excessive flow.

During our work on the flow model of MPFRAP, we determined that the range of velocities which can be accurately determined by MPFRAP, even with our new model, was well above the range of velocities believed to be exhibited by tracer molecules extravasating from leaky tumor vessels (Chary and Jain, PNAS 1989) (see Figure 3). In other words, we have determined that MPFRAP *cannot* be used to determine relative contribution of convection versus diffusion in transport out of a tumor vessel, which is the goal of task 7B and 7C. However, it has already been shown in the literature that diffusion dominates the extravasation of macromolecules from tumor vessels, over convection: this task was designed to *confirm* the literature determination in a less invasive manner. Now that we have determined that we cannot confirm the literature findings with this technique, I have decided to cease pursuing this question. To confirm the published literature in our laboratory without MPFRAP would involve extensive time and resources to establish the previously-used vessel cannulation techniques and would only add new insight in the unlikely case that we produced different results from previous measurements of Chary et al., using the same techniques. This is not a productive strategy for a young investigator. I am therefore planning to *believe* the literature finding that diffusion dominates over flow in tumor vessel extravasation, and move forward with the other aims in our proposal. Therefore this Task is completed.

Figure 3. Results from a simulation of the application of the flow model in the presence of typical experimental noise. The arrow indicates the scaled velocity when the tracer is 2M MW Dextran and interstitial flow is 0.6  $\mu\text{m/s}$  as determined by Chary et al. This is an order of magnitude too small to estimate with MPFRAP using the new flow model, as evidenced by the fact that the blue line has deviated from one, indicating the fit  $v$  does not equal the input  $v$ . The analogous scaled velocity for FITC-BSA is off of the curve entirely.



## **Progress on Task 9.**

Chronologically, the next Task in the Statement of Work is Task 9, which in its entirety is:

**Task 9.** Establish a reproducible measure of photodamage during a permeability measurement. (Years 1 and 2)

- A.** Evaluate systematic alterations in the fluorescence-versus-time curve as a reproducible measure of photodamage during permeability measurements.
- B.** Evaluate successive permeability measurements with distinct markers as a reproducible measure of photodamage during permeability measurements.
- C.** Evaluate second harmonic imaging of the adjacent matrix as a reproducible measure of photodamage during permeability measurements.

In pursuit of this task we chose to work on 9C first. We have determined that second harmonic imaging of the extracellular matrix provides a detailed readout of the structure of the collagen fibers

with a sensitivity to fibrillar structures below the resolution of light. The results of our investigation of the tumor extracellular matrix using SHG imaging have been published January of this year in Optics Express and that manuscript is attached to this report (as I am probably speaking to a general audience I should point out that Optics Express is currently tied for first place amongst optics journals, based upon impact factor). To summarize that work, we first evaluated the characteristic pitch angle  $\Theta$  of triple helices which assemble into collagen fibrils by analyzing the relationship between the angle of the incoming laser beam polarization relative to the fibril axis ( $\phi$ ), and the angle of the outgoing SHG polarization measured along two principle axes,  $I_x$  and  $I_y$ . Their relationship is derived in the attached manuscript and is given by:

$$\tan^2 \theta = \frac{2 \cos^2 \phi}{\sqrt{\frac{I_y}{I_x}} \sin(2\phi) - \sin^2(\phi)} \quad (1)$$

We found that in two different breast tumor cell lines (4T1 and TG1-1) grown in the mammary fat pad of immunocompetent mice, the characteristic pitch angle was the same across tumor types as well as between tumor collagen fibrils and healthy mammary fat pad fibrils, with  $\Theta \sim 52^\circ$ . This is somewhat surprising given the myriad differences between the healthy stroma and the tumor “reactive stroma” in terms of collagen production and composition.

We next evaluated the ratio between forwards-scattered SHG and backwards-scattered SHG using fresh thin slices of tumor tissue and careful calibration of our detection system with fluorescent beads of known F/B ratio. We again found that in two different breast tumor cell lines (4T1 and TG1-1) grown in the mammary fat pad of immunocompetent mice, the F/B ratio was the same across tumor types as well as between tumor collagen fibrils and healthy mammary fat pad fibrils, with  $F/B \sim 34$ . This F/B ratio measures the characteristic length scale (along the laser axis) over which the scattering material (i.e. collagen) is sufficiently ordered to produce SHG. This translates into a characteristic fibril diameter of  $\sim 70$  nm, common across both tumor types and healthy mammary fat pad. The fact that this fibril diameter is conserved between tumor and healthy tissue is surprising considering the elevated matrix degrading enzymes found in tumor “reactive stroma”. This suggests that the collagen fibrils that are sufficiently ordered to produce SHG signal are somehow protected from the altered degradative environment of the tumor reactive stroma.

With this work we have therefore established that SHG is an exquisitely sensitive measure of matrix structure, with the ability to measure structural properties (angle of assembly and fibril diameter) below the wavelength of light. We will therefore plan to utilize SHG F/B ratio imaging and  $\Theta$  measurements as a measure of photodamage of the ECM during permeability measurements, which was the original goal of this task. The measurement of the F/B ratio *in vivo* is a technical challenge, as the forward-scattered signal, by definition, will travel on into the tumor. However, last year we “spun off” a separate project based upon our preliminary work on Task 9, now funded by a Pew Scholar in the Biomedical Sciences Award, which is developing a technique to measure the F/B ratio with only backwards detectors. By the time our other tasks are regularly producing *in vivo* permeability data, and

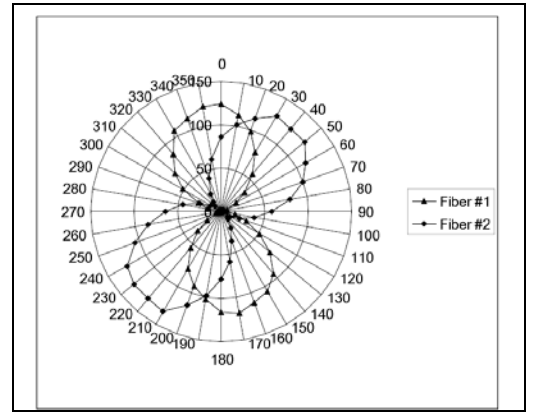


Figure 4. Radar plot of detected intensity versus analyzer angle. This represents the intensity versus analyzer angle for each of two selected fibers. In combination with the measured angle of the fiber relative to the laser polarization,  $I_x$ ,  $I_y$ , and hence  $\theta$  can be extracted from this data for each fiber.



hence need occasional checks on photodamage, this new technique will be on line and able to provide that information. Therefore this Task is completed.

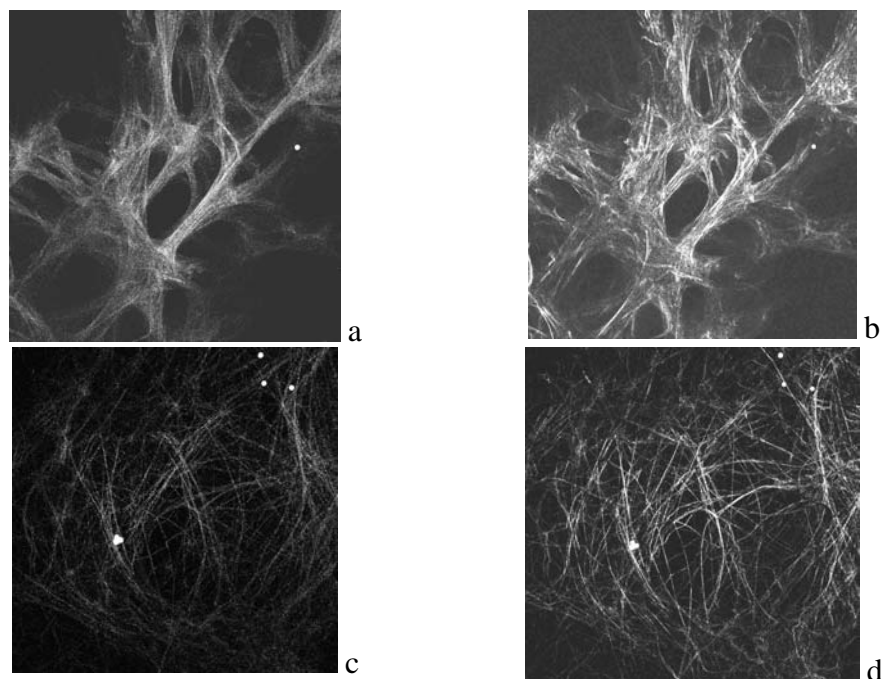


Figure 5. Top Row: a) Backwards-, and b) Forwards-scattered image of collagen in an acute slice of a TG1-1 mammary adenocarcinoma. Bottom Row: c) Backwards-, and d) Forwards-scattered image of collagen in an acute slice of a healthy mammary fat pad. The small dots in the images are calibration beads. Images are 680 microns across.

### **Progress in Task 8.**

Chronologically, the next Task in the Statement of Work is Task 8, which in its entirety is:

**Task 8.** Establish the allowed volume for accurate permeability measurements in the parameter space of i) average vessel permeability, ii) average tissue diffusion coefficient of fluorescent tracer, and iii) mean distance between vessels. (Years 2 and 3)

- A. Perform extensive mathematical modeling to determine the allowed volume in parameter space.
- B. Perform measurements of permeability, diffusion coefficients, and intravessel distances in tumor vessels to test the predictions of the model.
- C. Determine where in parameter space, on average, several key experimental tumor types lie.

The most significant portion of this task, Task 8A, was completed in year 2, where we performed mathematical modeling and demonstrated the ability to determine the safe intravessel distance for permeability measurements when the interstitial diffusion coefficient was known (via FRAP). The next significant portion of this task is 8C, wherein we determine the location in the 3D parameter space (permeability/diffusion coefficient/intravessel distance) of our experimental tumors. We put this task on hold this year, because we wanted to explore questions of saturation and desensitization in our experimental tumors (see below). This meant that we were unsure which tumor types to study for this task, and it seemed wise to wait until we had determined that. We have recently done so, settling on TG1-1 (ironically, our original choice in the initial proposal) and MCalV as two tumor types, both

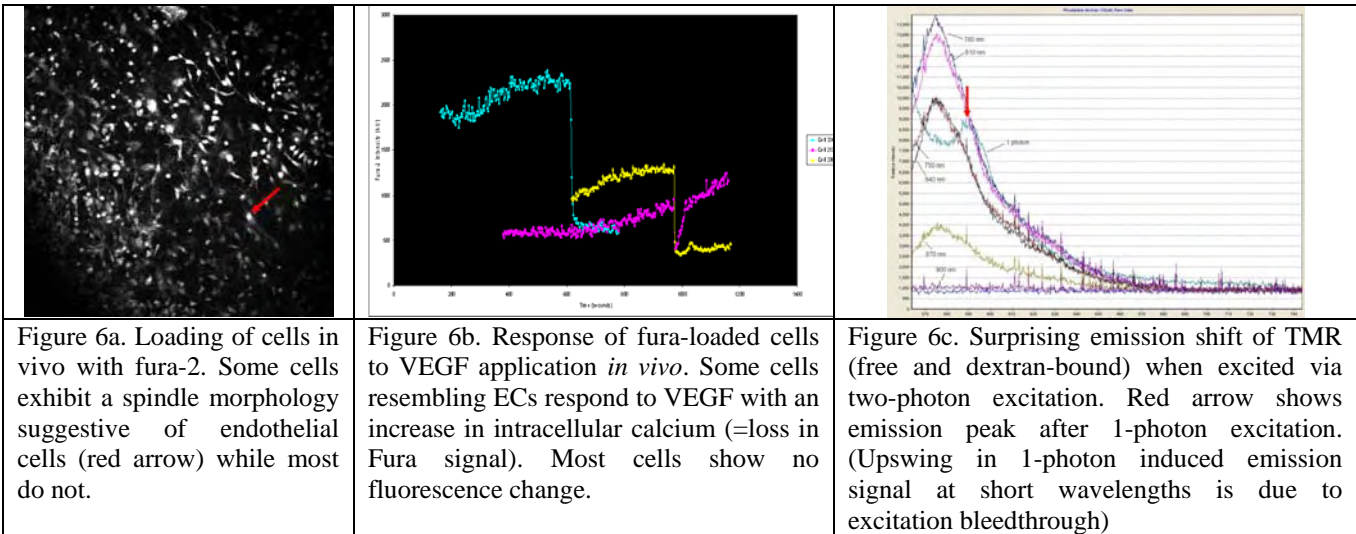
murine, with widely divergent levels of basal VEGF expression. We will now restart this task, and study those two tumors' location in parameter space to ensure safe permeability measurements. This Task is hence behind schedule.

### Progress in Tasks 1-6

Chronologically, the next tasks in the Statement of Work are Tasks 1 and 2. However, Tasks 1-6 all share several common features which we will discuss first:

Dorsal skinfold chambers: Generating dorsal skinfold chambers in sufficient numbers was a key stumbling block in years 1-2. While some of our laboratory members showed some skill in creating chambers, some we unable to master the technique. In year 3 we hired and trained a technician who has now become proficient at this surgical preparation.

Loading ECs *in vivo* with fluorescent calcium indicator dye. Generating consistent, reproducible loading of identifiable endothelial cells within a tumor with a calcium indicator dye was a significant hurdle in years 1-2, and remained somewhat problematic through year 3. After extensive manipulation of recipes and loading strategies, we were able to load Fura-AM into cells in the upper ~100 microns of the dorsal skinfold chamber with topical application of loading solution (see Figure 6a). Some of these cells indeed demonstrated a fluorescence response to application of VEGF to the tumor surface (see Figure 6b). However, we are not convinced that we will be able to unequivocally identify the cells loaded with Fura as endothelial cells based upon their location adjacent to vessels loaded with TMR-Dextran via i.v. injection. This is because of the surprising green shift in emission of TMR-Dextran under two-photon excitation (see Figure 6c), as well as its overall extremely dim signal on our system. As a result, we have recently been exploring Fura-red loading combined with FITC-Dextran as a vessel marker. FITC-Dextran is extremely bright and has minimal cross-talk in the Fura-red emission channel. This color combination has the added benefit that when we study one of our chosen tumor cell lines, the TG1-1 line (originally from the FVB strain of inbred mice), we can grow it in the TIE2-GFP mouse (FVB strain) from Jackson labs, where the endothelial cells express GFP.



Stable perfusion of reagents. Our initial method of manual pipetting produced excessive sample motion. This was solved last year with the purchase of, and practice with, a multichannel perfusion system

Saturation and desensitization. Analysis of the literature on the mechanisms of EC responses to VEGF reveal that the relevant data is generated in healthy ECs, where extrinsic VEGF is added to a background of little or no VEGF. However, in tumors, the ECs exist in a steady-state elevated level of VEGF. Therefore we realized that an integral part of our project is to understand how ECs behave in the presence of steady elevations of VEGF, how they respond to alterations in VEGF concentrations from a non-zero baseline, and how these behaviors compare to *the same* ECs responding to extrinsic VEGF in the absence of baseline elevated VEGF. VEGF receptors (VEGFR) belong to the tyrosine kinase family of receptors. Upon exposure to their specific ligand, these receptors can become refractory to subsequent activation by endocytic downregulation, whereby receptor-ligand complexes are internalized, or by desensitization, the uncoupling of the receptor from the signaling machinery. The molecular basis for endocytic downregulation in the tyrosine kinase family of receptors is best characterized for epidermal growth factor (EGF) receptors, but VEGFR endocytosis has also been demonstrated. In the tumor microenvironment constitutive production of VEGF may lead to attenuation of the VEGFR signaling pathway, and TPLSM will be a powerful tool to determine if tumor EC exhibit an attenuated VEGF response *in vivo*. This has important implications for the treatment of tumor endothelial cells with VEGF inhibitors.

To begin to address this issue, we asked if VEGFR signaling was attenuated in normal EC by measuring HUVEC calcium responses with our *in vitro* perfusion system. HUVEC were incubated for 18 h with 20 ng/ml VEGF in endothelial cell basal medium (EBM) containing no fetal calf serum or other growth factors. Negative controls included cells incubated with 20 ng/ml bovine serum albumin (BSA) in EBM or EBM alone. After 18 hours the cells were washed and loaded with Fura-2. Fluorescent intensity in Fura-2-labeled HUVEC perfused with either Puck's saline or VEGF (20 ng/ml) were measured over time. Fig. 7(A-I) depicts responses of HUVEC from the same experiment. Preexposure to VEGF did not alter baseline fluorescent intensity determined by imaging during perfusion with Puck's saline (Fig. 7A-C). The response to 20 ng/ml VEGF with VEGF preexposure is attenuated (Fig. 7G-I) compared to cells not preexposed to VEGF (Fig. 10B). The maximal response as a percentage of baseline is shown in Fig. 8. For the baseline response, cells preexposed to EBM or 20 ng/ml BSA and imaged with Puck's saline were not different from each other (data not shown), and the data from these negative controls were combined in Fig. 8. Statistical analysis with Tukey's post-hoc test determined that the response to VEGF with no VEGF preexposure is significantly different from all other groups, including VEGF response in cells preexposed to VEGF. Using this conservative post-hoc analysis, the VEGF preexposed cells imaged in VEGF did not differ from the cells exposed to EBM and imaged in Puck's saline, but a larger n may lead to a significant difference between those two groups. Unlike a primary exposure to VEGF, cells reexposed to VEGF showed a delayed time to the maximal VEGF response, ranging from 530 to 720 s in 3/5 experiments. The response was very gradual, and the maximum response was difficult to estimate in 2/5 experiments. This long gradual increase in calcium is more similar to that observed at 5 ng/ml VEGF, and is in contrast to the rapid onset of calcium entry upon a cell's initial encounter with higher doses of VEGF. These results demonstrate that normal EC exposed to VEGF are refractory to subsequent VEGF signaling.

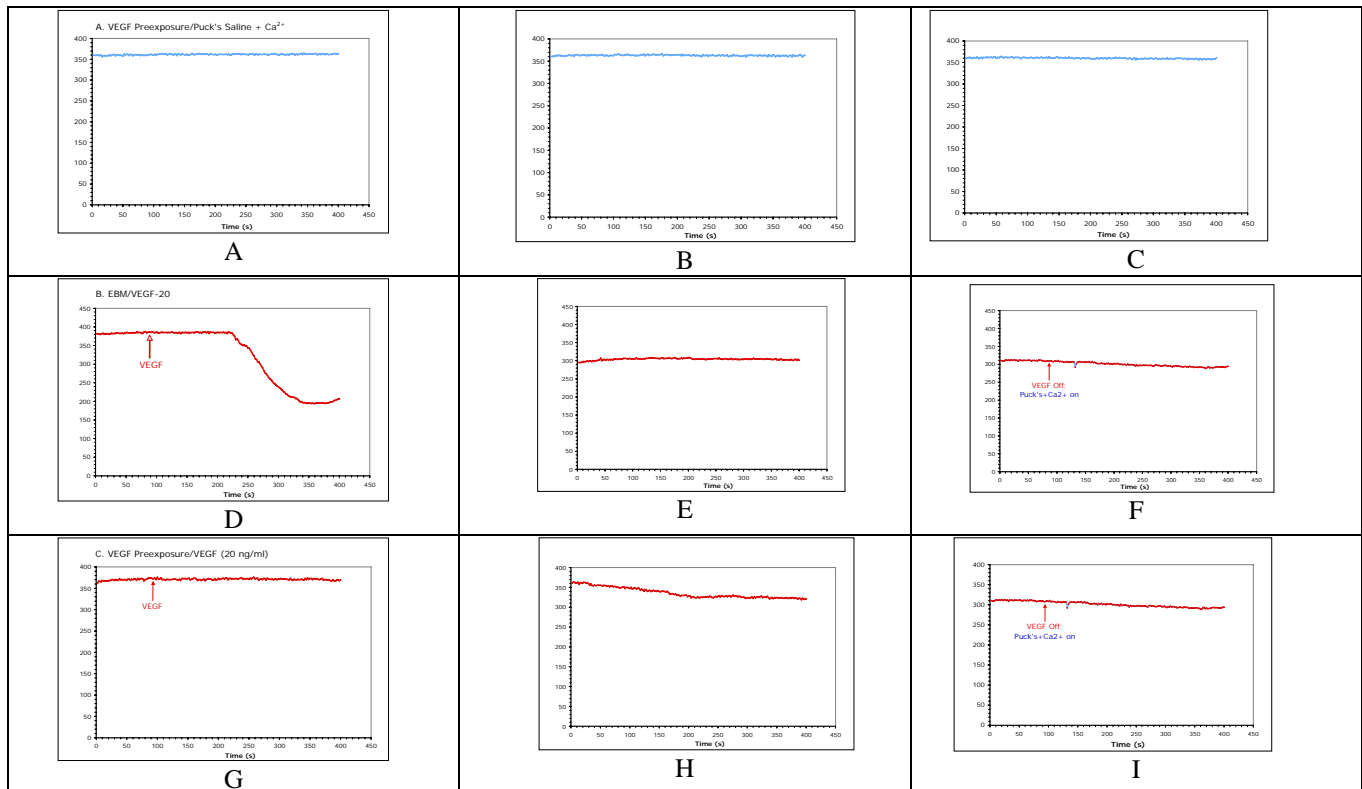
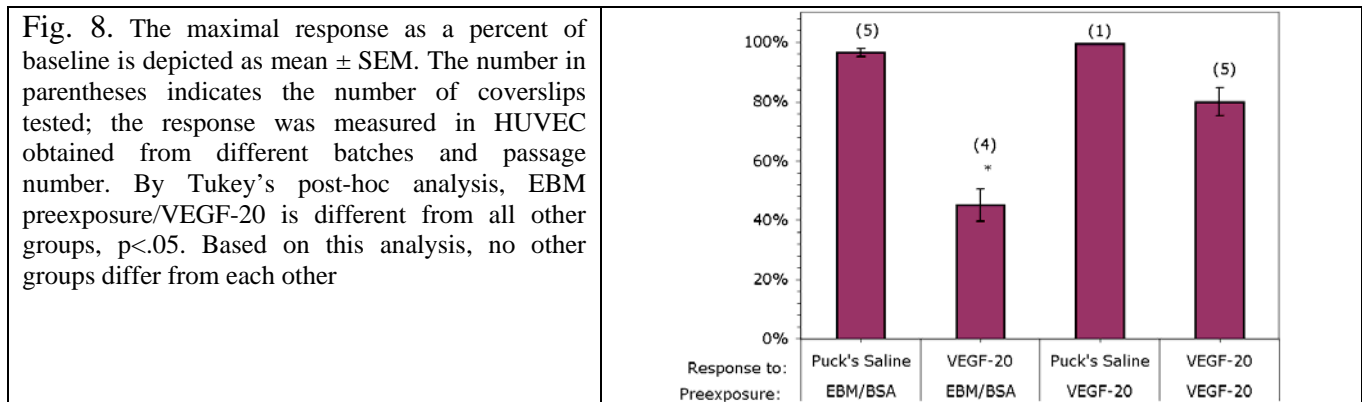


Fig. 7.  $\text{Ca}^{2+}$  influx is attenuated with secondary exposure to VEGF. HUVEC were incubated in endothelial basal medium (EBM) for 6 h followed by EBM, 20 ng/ml BSA or 20 ng/ml VEGF for 18 h at 37°C. Fluorescent intensity was measured during continuous perfusion with Puck's saline or 20 ng/ml VEGF. Representative responses shown: VEGF preexposure/imaging in Puck's saline (A-C), EBM or BSA preexposure/imaging with VEGF (D-F), VEGF preexposure/imaging with VEGF (G-I).



We have therefore shown that the response of healthy ECs to extrinsic VEGF is altered by their pre-exposure to VEGF. We are going to continue to explore this effect *in vitro*, but we also felt that it was important to choose tumor cell lines for our originally planned *in vivo* studies (Tasks 1-6) which have widely varying levels of baseline VEGF expression, in order to explore as wide a range of saturation/desensitization states as possible. Therefore we assayed VEGF by sandwich ELISA and standardized to the total amount of protein present. The five tumors assayed exhibit highly disparate growth rates, and therefore tumors were controlled by size (10-12 mm, long axis) as opposed to age. All tumors were derived from orthotopic injection of  $1 \times 10^5$  cells in the mammary fat pad of healthy female mice of appropriate strain. Tumors were grown to size and resected before being homogenized. Cell lysates were spun to remove debris and supernatants subjected to sandwich ELISA in duplicate.

Two to three tumors were assayed from each tumor line. The results are shown in Figure 9. In order to explore the signaling pathway translating VEGF receptor activation to permeability alterations (our Tasks 1-6), but do so over a range of background VEGF levels, we therefore want to choose from Figure 9 two different tumor types with very different levels of VEGF, preferably including one that has very low VEGF to ensure that there is a response to extrinsic VEGF. We also would prefer to confine our studies to tumor types from the same species, i.e. study two human tumor cell lines or two murine cell lines. As shown in Figure 9, both of the human tumor cell lines that our lab has familiarity with (MDA-MB-231 and MDA-MB-3361) exhibit relatively high levels of baseline VEGF, as does the murine mammary adenocarcinoma MCAIV. However the murine cell lines 4T1 and TG1-1 both exhibit relatively low baseline VEGF. As TG1-1 can be grown in TIE2-GFP mice (FVB background) and hence have its TEC's intrinsically fluorescent with GFP, we are proceeding with Tasks 1-6 using MCAIV (high VEGF) and TG1-1 (low VEGF) in order to address the fundamental questions of this grant in the context of widely varying background VEGF levels.

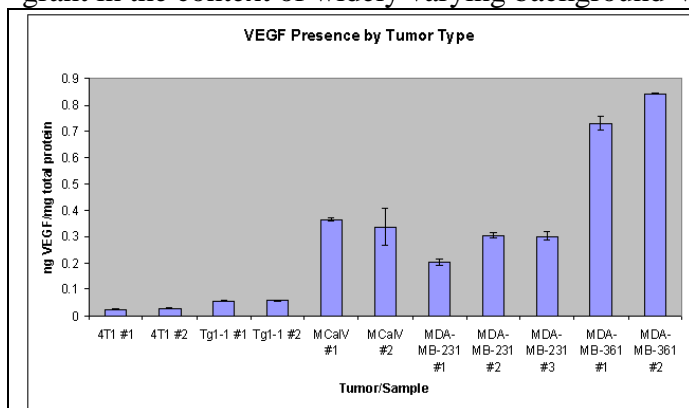


Figure 9. Baseline VEGF levels in five different tumor cell lines evaluated with ELISA. The MCAIV and TG1-1 cell line pair provide a 6x variation in VEGF levels, within a common host species (mouse), while allowing some use of the TIE-2 GFP mouse (for the TG1-1 tumors). MCAIV and 4T1 provide a higher variation in VEGF levels (13x) but preclude any use of the TIE-2 GFP mouse, while the MDA-MB-231/361 pair provide only a 3x variation in VEGF.

These accomplishments contribute to all of the remaining Tasks in this grant (Tasks 1-6). We can now return to a task-by-task discussion of progress over the preceding year.

### **Progress in Task 1.**

Chronologically, the next Task in the Statement of Work is Task 1, which in its entirety is:

**Task 1.** Determine role of external calcium influx on translation of VEGFR2 activation to tumor endothelial cell (TEC) calcium signals and tumor vessel permeability. (Year 3)

- A. Apply NiCl (blocks plasmalemmal calcium channels) and CaCl<sub>2</sub> to a tumor vessel via pipette and observe the TEC calcium response and subsequent permeability change.
- B. Elevate TEC calcium and vascular permeability with extrinsic VEGF then attempt to block this elevation by repeating with NiCl.
- C. Reduce TEC calcium and vascular permeability with VEGF blockade and attempt to recover baseline calcium and permeability with CaCl<sub>2</sub>.

We have made extensive progress in this task, albeit in *in vitro* applications, as we have only recently finalized our *in vivo* loading preparation and chosen our two cell lines for study. We have imaged VEGF-induced changes in cytosolic calcium in bovine aortic endothelial cells (BAEC) and in human umbilical cord endothelial cells (HUVEC) *in vitro* using the fluorescent calcium indicator dye, Fura-2 AM and two photon laser scanning microscopy:

**Methods.** Commercially available HUVEC or BAEC grown on fibronectin-coated coverslips are growth factor- and fetal calf serum-deprived for 24 h prior to imaging. To load with Fura-2 AM, cells are incubated in Fura-2 AM for 45 min at 37°C, washed and incubated with Puck's saline for 10 min for 37°C prior to imaging. For imaging, the coverslip is placed in a dish attached to a perfusion system that delivers reagents at a constant flow rate with constant aspiration for continuous fluid exchange. The imaging buffer is Puck's saline (containing 136 mM NaCl, 5.36 mM KCl, 5.05 mM dextrose, 4.12 mM NaHCO<sub>3</sub>, 1.25 mM MgSO<sub>4</sub>

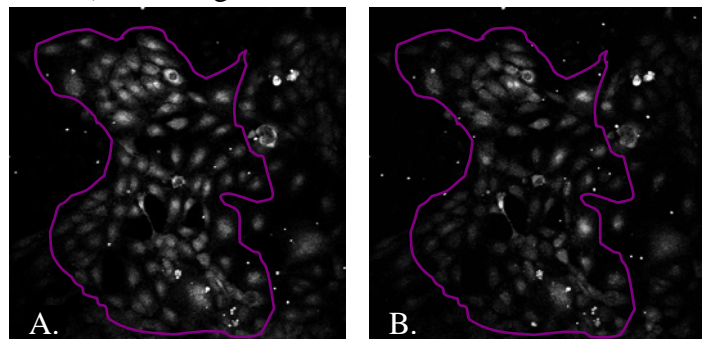


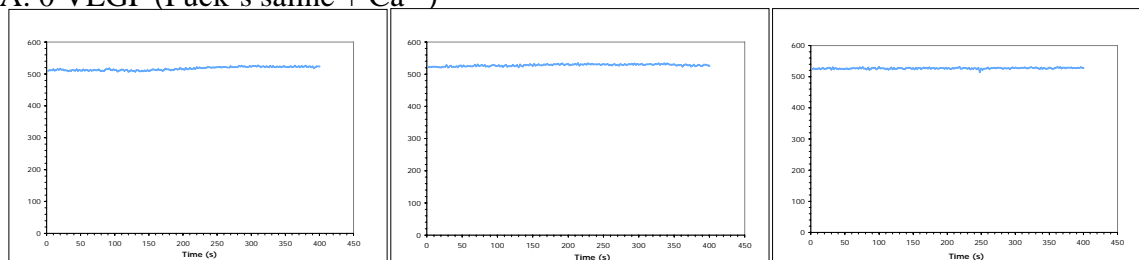
Fig. 10. Fura-2-loaded HUVEC exposed to Puck's saline (A) and 310 s after exposure to 20 ng/ml VEGF (B).

with or without 1.6 mM Ca<sup>2+</sup>). (All reagents were dissolved in Puck's saline). The cells are scanned by a pulsed, high intensity red laser (810 nm excitation wavelength) every 2 sec with 0.9 s rest between scans. Fluorescent emission (535/40 nm) is detected with a photomultiplier tube. Laser power exiting the objective lens ranged between 20-30 mW. For each scan, the average fluorescent intensity in a region of interest (ROI) consisting of groups of cells (as in Fig. 10) is determined using NIH Image J software.

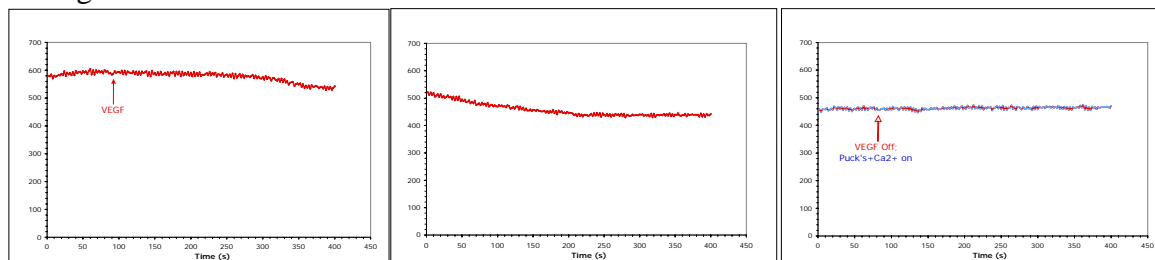
**Results.** Representative cytosolic calcium changes in HUVEC in response to 0, 5, 20, and 100 ng/ml recombinant human VEGF<sub>165</sub> (VEGF) are shown in Fig. 11. Fig. 11A shows that fluorescent intensity is stable with continuous exposure to Puck's saline. With 5 ng/ml VEGF, a gradual and shallow decrease in fluorescent intensity is observed with no evidence for even a partial return of cytosolic calcium to baseline (increased fluorescent intensity) at any time throughout the imaging session (Fig. 11B). In contrast, 20 and 100 ng/ml VEGF (Fig. 11C, D, respectively) initiated a rapid peak in cytosolic calcium and a partial return to baseline in the presence of VEGF or upon removal of VEGF. The magnitude of the response and the time to the maximum response was calculated as described in the legend to Fig. 12. The magnitude of the response is equivalent between 20 and 100 ng/ml and greater than 5 ng/ml VEGF (Fig. 3A). The time required to generate a maximal response is reached more quickly with 20 and 100 ng/ml VEGF compared to 5 ng/ml (Fig. 12B). It should be noted that the responses shown in Fig. 12 were averaged across different HUVEC batches and passage number (between 2 and 7).

These results show that the kinetics of the calcium response to VEGF is dependent on VEGF concentration. At higher concentrations of VEGF, a transient, rapid increase in calcium is followed by a sustained elevation of calcium relative to baseline, while lower VEGF concentrations elicit a slow but sustained increase in cytosolic calcium that does not return to baseline during the imaging period.

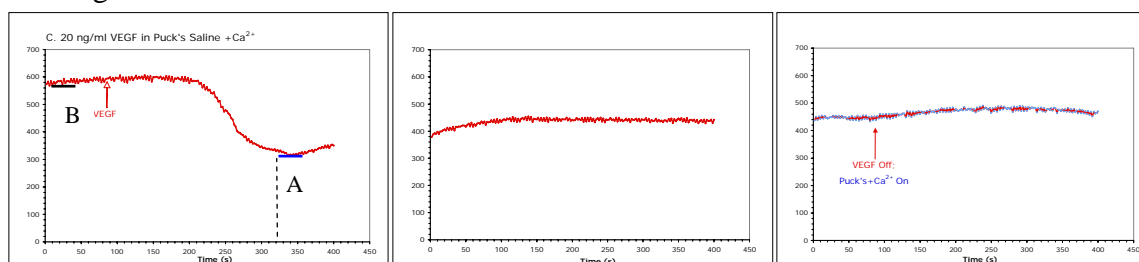
### A. 0 VEGF (Puck's saline + $\text{Ca}^{2+}$ )



### B. 5 ng/ml VEGF



### C. 20 ng/ml VEGF



### D. 100 ng/ml VEGF

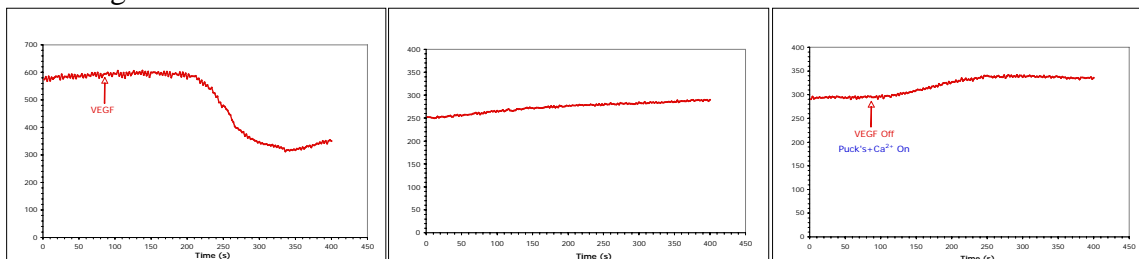


Fig. 11. Cytosolic  $\text{Ca}^{2+}$  responses to varying VEGF concentrations. HUVEC loaded with the cell permeant fluorescent calcium indicator dye, Fura-2 AM were imaged during continuous perfusion of Puck's saline or VEGF. Mean fluorescent intensity for each scan is graphed as a function of time (s). Entry of reagent into the dish is indicated by an arrow.

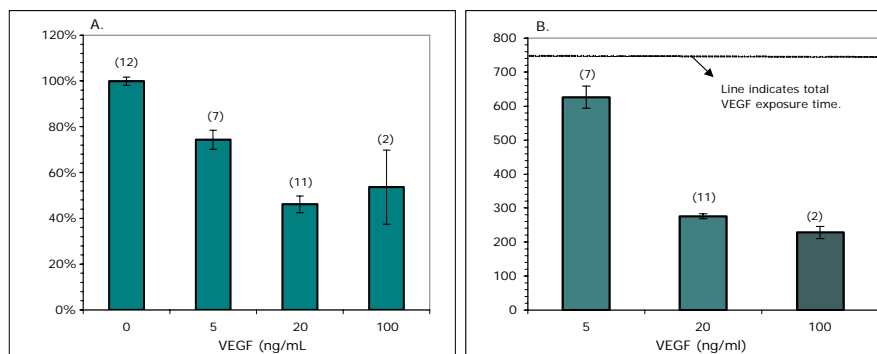


Fig. 12. Quantification of HUVEC  $\text{Ca}^{2+}$  responses. The maximum response (A) is calculated by dividing the average fluorescent intensity determined at the lowest point in the VEGF response (line A in Fig. 2C; n = 15 scans) by the average fluorescent intensity at baseline (line B in Fig. 2C; n = 15 scans) and multiplying by 100. The time to maximum response (B) was the earliest time at nadir (vertical line, Fig. 2C). The results shown are mean  $\pm$  SEM; n in parenthesis is the number of coverslips tested. In (B) the total time cells are exposed to VEGF is represented by the dotted line.



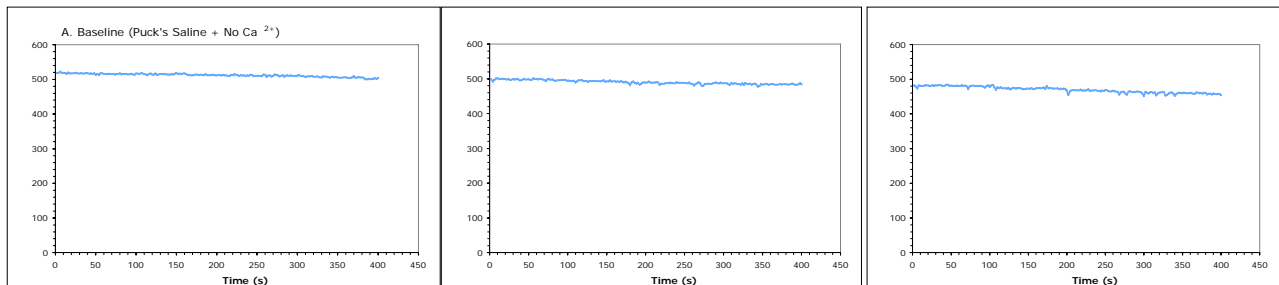
Calcium can enter the cytosol from outside the cell or it can be released from internal stores. Our objective was to estimate the relative importance of extracellular versus intracellular calcium in determining the magnitude and duration of the response to VEGF in normal and tumor EC. To examine the role of calcium entry from the extracellular fluid, the calcium response to VEGF was measured in Puck's saline containing no calcium (Fig. 13). In the absence of external calcium, the response to 20 ng/ml VEGF is blunted and is rapidly and fully restored to baseline (Fig. 13B) compared to the response in the presence of external calcium (Fig. 13C). Note that the restoration to baseline occurred with continued VEGFR signaling – that is, in the presence of VEGF. Fig. 14 shows the magnitude of the response, expressed as percent of baseline, is greatest with external calcium (Fig. 14A), and the time to the maximum response is somewhat slower (Fig. 5B).

These results show that calcium entry from the extracellular environment contributes to the magnitude of the calcium response, but intracellular stores may also determine the magnitude of the initial peak calcium response. The complete restoration of calcium levels to baseline observed in the absence of external calcium suggests that the sustained elevation above background is completely dependent on extracellular calcium. The transient increase in calcium observed in the absence of external calcium suggests input from release of intracellular stores. Interestingly, this distinct transient calcium peak observed in HUVEC (Fig. 13B) is not observed in BAEC in the absence of extracellular calcium following stimulation with 20 ng/ml (Fig. 15B) or 100 ng/ml VEGF (data not shown). Therefore, although BAEC display a similar kinetic response to VEGF in external calcium (Fig. 15A), the molecular mechanisms underlying the cytosolic calcium response may differ somewhat between the two types of EC. We have also observed that the magnitude of the maximal response to VEGF is reduced in BAEC compared to HUVEC (Fig. 12A compared with Fig. 16A), although the time to the maximum response is equivalent (Fig. 12B compared to Fig. 16B). This difference may be a species difference (bovine VEGFR responding to human VEGF) or it may be a reflection of heterogeneity within EC.

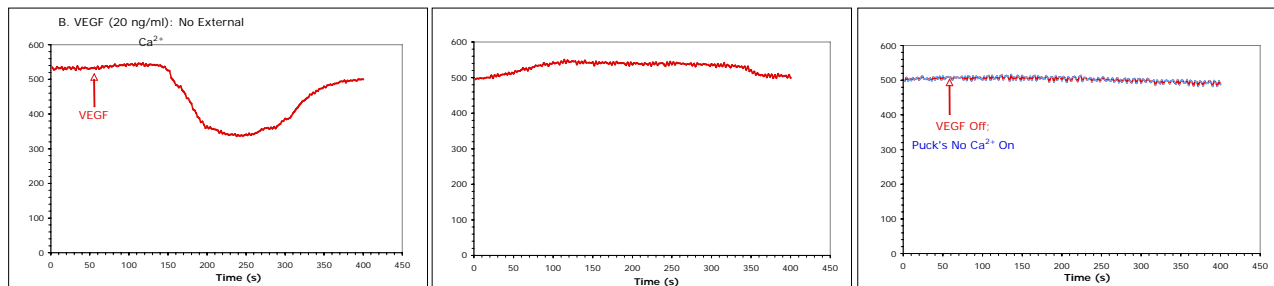
In summary, we have evaluated the role of external calcium influx on VEGF signaling *in vitro*, but have not extended this work *in vivo* into the living tumor. We are therefore slightly behind schedule on this Task.



### A. Baseline (Puck's Saline + No $\text{Ca}^{2+}$ )



### B. 20 ng/ml VEGF; No external $\text{Ca}^{2+}$



### C. 20 ng/ml VEGF + External $\text{Ca}^{2+}$

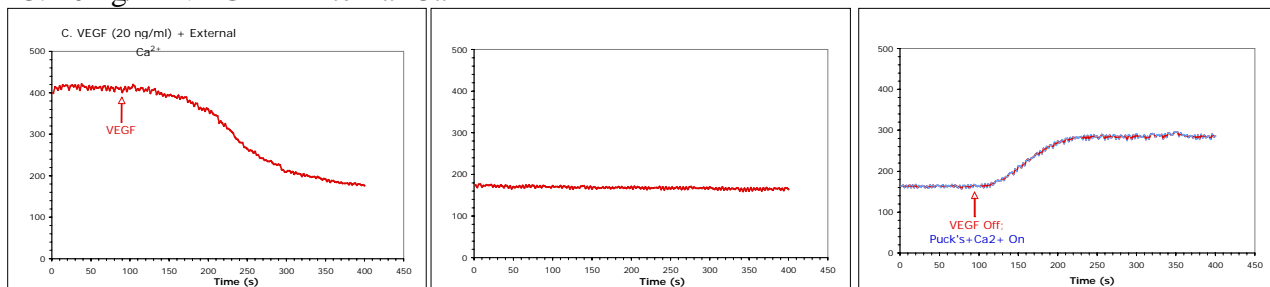


Fig. 13. The calcium response to VEGF requires external  $\text{Ca}^{2+}$ . HUVEC were imaged with continuous exposure to A) Puck's saline with no calcium, B) 20 ng/ml VEGF in Puck's saline with no calcium, and C) 20 ng/ml VEGF in Puck's saline containing 1.6 mM calcium. The results shown are all from the same imaging session.

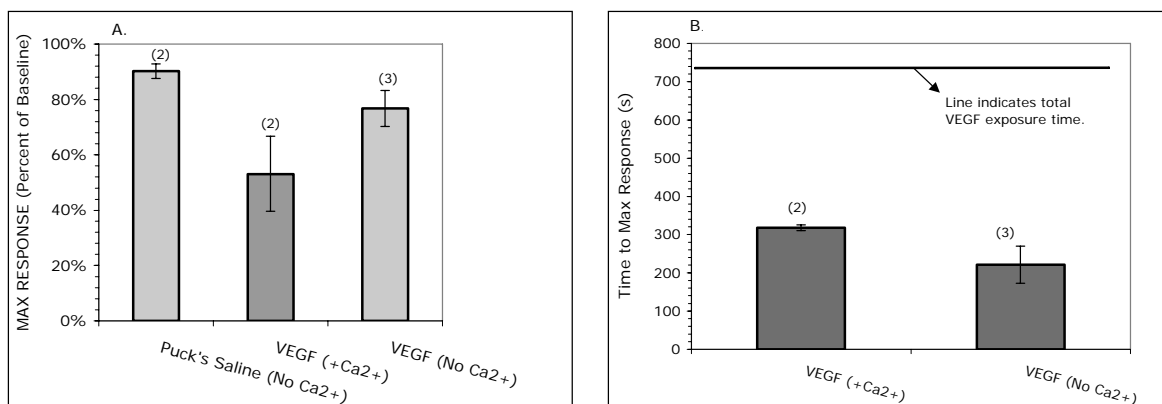
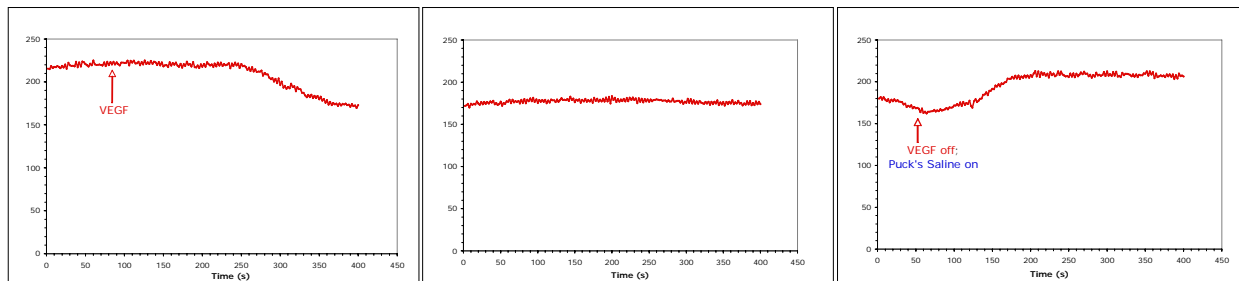


Fig. 14. Calcium response in HUVEC continuously exposed to VEGF dissolved in Puck's saline with and without 1.6 mM  $\text{Ca}^{2+}$ . The maximum response (A) and the time to maximum response (B) were determined as described in Fig. 3. The results are mean  $\pm$  SEM; the number of coverslips tested is shown in parenthesis.

### A. 20 ng/ml VEGF + 1.6 mM $\text{Ca}^{2+}$



### B. 20 ng/ml VEGF, No external $\text{Ca}^{2+}$

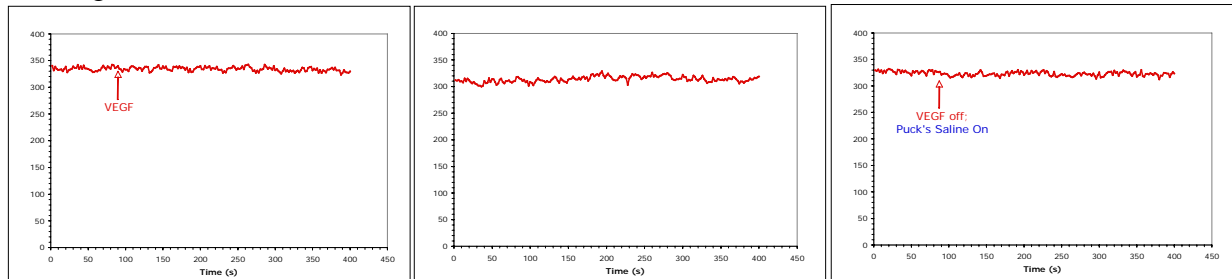


Fig. 15. Representative BAEC cytosolic  $\text{Ca}^{2+}$  responses to VEGF with and without external calcium. BAEC were imaged during continuous exposure to 20 ng/ml VEGF in the presence of 1.6 mM calcium (A) compared to 20 ng/ml VEGF in the absence of external calcium (B). The results shown are from the same imaging session.

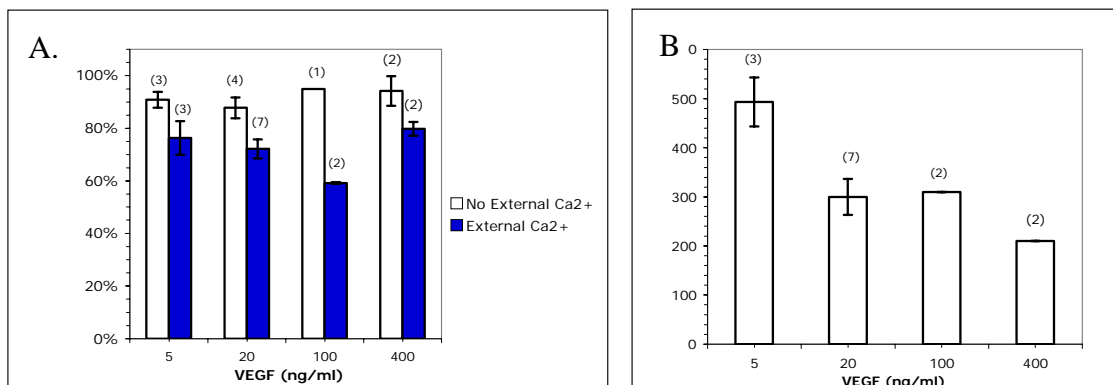


Fig. 16. Quantification of the  $\text{Ca}^{2+}$  response to varying doses of VEGF in BAEC. The maximum response as a percent of baseline (A) and the time to the maximum response (B) were calculated as described in the legend to Fig. 3. The responses were determined using different BAEC batches and passage number. The results are shown as mean  $\pm$  SEM; the number in parenthesis indicates the number of coverslips tested. Note that 100 ng/ml VEGF is optimal for the maximum calcium response in BAEC compared to 20 ng/ml in HUVEC (Fig. 3A). Responses in no external calcium differ from responses in external calcium,  $p < .05$ , Tukey's post-hoc analysis.

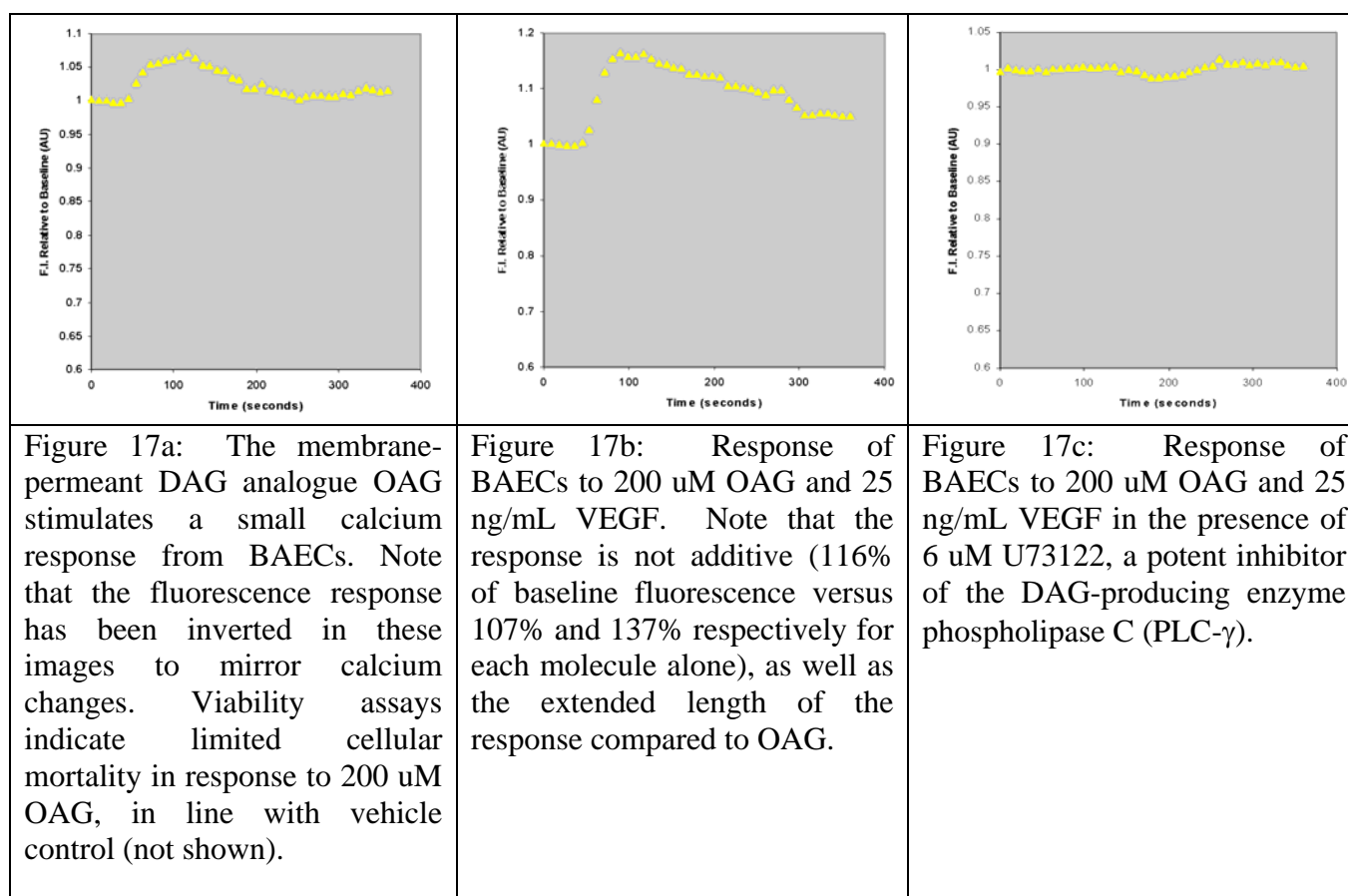
## **Progress in Task 2:**

The next task in the original Statement of Work is Task 2, which in its entirety is:

**Task 2.** To determine the role of diacylglycerol (DAG) in translation of VEGFR2 activation to TEC calcium signals and tumor vessel permeability. (Year 3)

- A.** Apply OAG (a DAG analog) and U73122 (a PLC $\gamma$  inhibitor) and observe the calcium response in TECs as well as monitor subsequent vascular permeability changes.
- B.** Elevate TEC calcium and vascular permeability with extrinsic VEGF via pipette administration, and attempt to block this elevation by repeating with DAG inhibitor.
- C.** Reduce TEC calcium levels and vascular permeability with VEGF blockade, and attempt to recover baseline TEC calcium and vascular permeability with OAG.

The following series of figures indicates the effect of the presence and absence of the second messenger DAG on VEGF-induced calcium influx in BAECs:



In these *in vitro* experiments, performed in a plate reader, we see that the membrane-permeable DAG analogue OAG produces calcium transients in the absence of VEGF. This effect is not additive with transients produced by VEGF alone (figure 17b). Surprisingly, a PLC-g inhibitor, U73122m inhibits response to OAG and to VEGF. OAG should recover the response to VEGF in the presence of U73122 by crossing the cell membrane and taking the place of DAG, but this response is curiously absent in this assay. This assay has been performed with this combination of reagents four times, with no response evident from BAECs. Cellular viability is in line with vehicle-only controls (not shown).

The failure of the cells to recover a VEGF-induced calcium influx while both in the presence of OAG and the U73122-induced absence of DAG is a point that will have to be examined further prior to this particular reagent combination being used *in vivo*. However, OAG alone and OAG in concert with VEGF produce a long-term calcium elevation easily seen in Figures 17a and 17b, and these reagents should prove equally effective in the mouse model. An interesting possibility is raised by the relationship of the calcium response to VEGF alone (Figure 15), the response to OAG alone (Figure 17b), and the two together (Figure 17c). The responses are not additive, indicating the possibility that the cellular machinery has reached a saturation point (a state in which response to the signaling pathway is curtailed by endocytosis of receptors, destruction of second messengers, inactivation of key enzymes, etc.). As the availability of VEGF *in vivo* to TEC is likely not to be a rate-limiting factor in this signaling cascade due to the cytokine's prevalence in the tumor microcirculation, it is possible that many types of TEC will exhibit saturation of this particular signaling pathway *in vivo*. In this situation, responses to VEGF and OAG seen in serum-deprived EC will not be evident, as the cellular machinery charged with transducing such responses will be functionally downregulated. It is for this reason that we evaluated the native VEGF production of several tumor types in order to choose two with widely varying VEGF levels.

In summary, we have performed extensive *in vitro* assays for the role of DAG in VEGF signaling, but have not yet implemented it *in vivo*. Hence, this task is slightly behind schedule.

### **Progress in Task 3.**

Task 3 is scheduled to begin next year, but we have already made some progress. In its entirety, Task 3 is:

**Task 3.** To determine the role of IP3 activated release of calcium from internal stores in translation of VEGFR2 activation to TEC calcium signals and tumor vessel permeability. (Year 4)

**A.** Apply Ip3, xestospongine (an IP3R blocker), and thapsigargin (permanently drains the external stores) to tumor vessels via pipette and observe the TEC calcium response and subsequent permeability change.

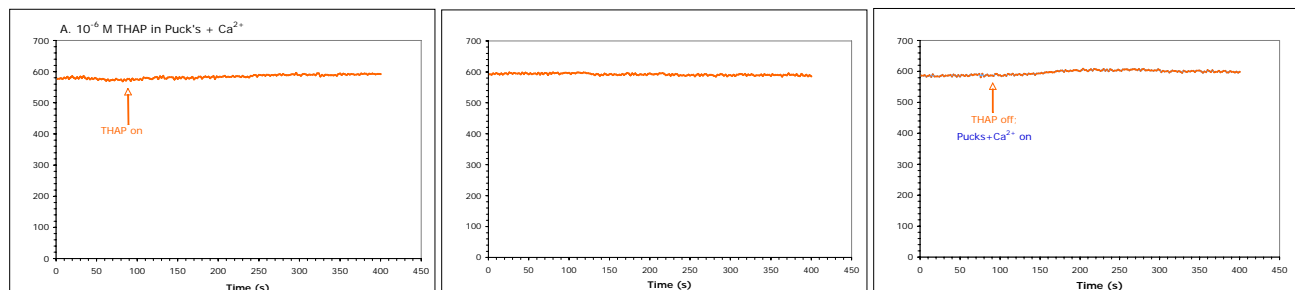
**B.** Elevate TEC calcium and P with extrinsic VEGF via pipette and attempt to block this elevation by repeating with xestospongine and thapsigargin.

**C.** Reduce TEC calcium and vascular permeability via VEGF blockade, and attempt to recover baseline calcium and permeability levels with IP3.

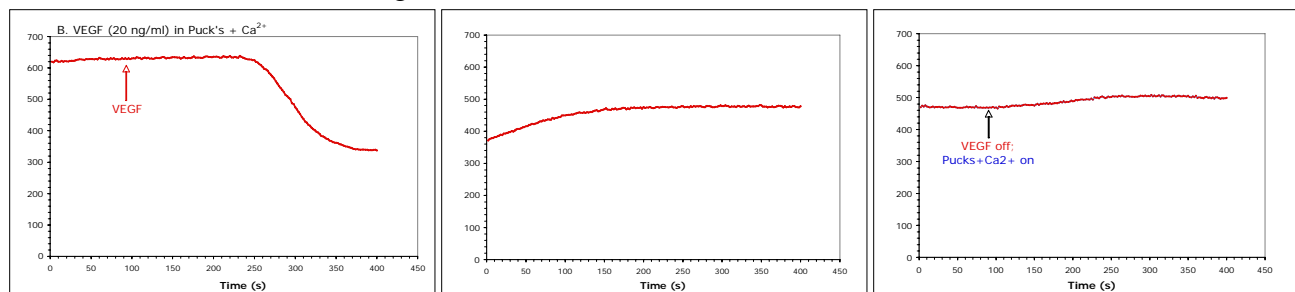
To examine the contribution of calcium released from internal stores to the VEGF calcium response, HUVEC were pretreated with thapsigargin for 30 min prior to imaging. Thapsigargin inhibits the uptake of calcium into smooth endoplasmic reticulum (SER), the internal storage site, and depletes calcium stores. Thapsigargin pre-treated cells were continuously infused with either thapsigargin (Fig. 18A) or thapsigargin + 20 ng/ml VEGF (Fig. 18C). The response to 20 ng/ml VEGF incubated with Puck's saline is shown in Fig. 18B. The magnitude of the VEGF-induced calcium response in thapsigargin-treated HUVEC is not significantly altered (Fig. 19A), suggesting a limited dependence on internal stores VEGF-induced calcium in determining the magnitude of the peak calcium response. The time to the maximum response varied considerably between the two coverslips tested (Fig. 19B), and it remains to be determined if the absence of internal stores delays the time to the maximal response.

In summary, we have made significant progress in evaluating the role of internal stores in VEGF signals *in vitro*, and have mastered the use of the relevant reagents and interpretation of the results. We are hence well prepared to apply these reagents *in vivo* and are ahead of schedule on this task.

### A. $10^{-6}$ M thapsigargin/ $10^{-6}$ M thapsigargin



### B. Puck's saline/VEGF (20 ng/ml)



### C. $10^{-6}$ M thapsigargin/ $10^{-6}$ M thapsigargin + 20 ng/ml VEGF

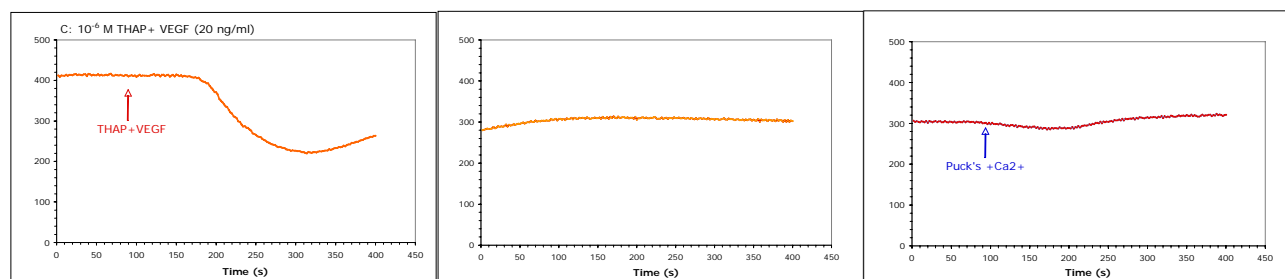


Fig. 18. Depletion of internal stores by thapsigargin pretreatment. Fura-2-loaded HUVEC were incubated with  $10^{-6}$  M thapsigargin (A,C) or Puck's saline (B) for 30 min at 37°C prior to imaging. Cells were imaged as described in Fig. 2 with continuous exposure to A)  $10^{-6}$  M thapsigargin, B) 20 ng/ml VEGF, and C)  $10^{-6}$  M thapsigargin + 20 ng/ml VEGF. The results shown are from the same imaging session.

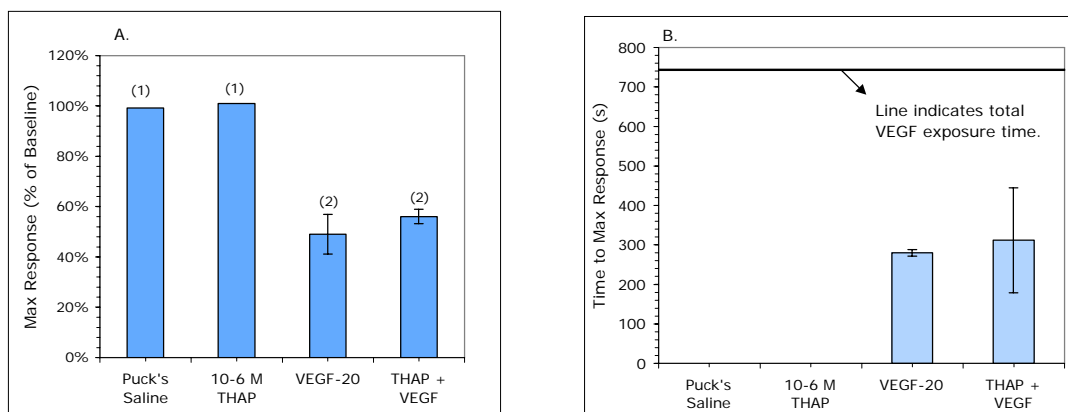


Fig. 19. Depletion of internal stores by thapsigargin pretreatment. The maximum response as a percent of baseline (A) and the time to the maximum response (B) were calculated as described in the legend to Fig. 3. Results are mean  $\pm$  SEM of n=1-2 coverslips.

### **Key Research Accomplishments in the Past Year**

- 1) We have completed Tasks 7 and 9, the two Tasks that were chronologically first.
- 2) We have made significant progress in Tasks 1 and 2.
- 3) We have begun work ahead of schedule on Task 3.
- 4) We have solved our problems with supply of surgical preparations.
- 5) We discovered the role that saturation and desensitization of receptors will play in our studies of VEGF signaling *in vivo*, and have accounted for those properties by evaluating the basal VEGF levels of several tumor types and choosing two widely varying types for our ongoing *in vivo* studies.

### **Reportable Outcomes**

Over the past year I have published one paper:

Han X, Burke R, Zettel M, Tang P, Brown E. (2008) Second harmonic properties of tumor collagen: determining the structural relationship between reactive stroma and healthy stroma. *Optics Express*. 16(3):1846-1859

This is also the first paper from my new laboratory and hence represents a significant milestone. Over the past year I have also submitted one additional paper for publication:

Sullivan K, Sipprell W, Brown E, Brown E. (2008) Improved model for multi-photon fluorescence recovery after photobleaching (MP-FRAP) expands the application of MP-FRAP within the *in vivo* environment. *Manuscript Submitted to Biophysical Journal*.

Over the past year I have also published two book chapters:

Brown E, Majewska A, Jain RK (2008) Photobleaching and Recovery with Nonlinear Microscopy. In: So P., Masters B. (eds) Handbook of Biological Nonlinear Optical Microscopy. Oxford University Press, Oxford UK. Chapter 26, pp. 673-688

Jain RK, Booth M, Padera T, Munn L, Fukumura D, Brown E. (2008) Applications of Nonlinear Intravital Microscopy in Tumor Biology. In: So P., Masters B. (eds) Handbook of Biological Nonlinear Optical Microscopy. Oxford University Press, Oxford UK. Chapter 29, pp. 735-756

Over the past year I have also filed one provisional patent application:

Dickerson I, Brown E. (2008) Methods of treating cancer using an agent that modulates activity of the calcitonin-gene related peptide ("CGRP") receptor. Provisional Patent Application 61/079,204

Over the past year I have given three invited talks:

"Studying the Tumor Extracellular Matrix using Second Harmonic Generation" Invited lecture presented at the Department of Physics, Wake Forest University, Winston-Salem, NC, 2007

"Applications of Multiphoton Laser Scanning Microscopy: Transport in Tumors" Invited lecture presented as the Homecoming Alumni Colloquium, Department of Physics, Wake Forest University, Winston-Salem, NC, 2007

“Multiphoton Fluorescence Recovery After Photobleaching in the Presence of Flow” Invited lecture presented at the Carl Ludwig Institute of Physiology, University of Leipzig, Leipzig, Germany, 2008

Over the past year I also chaired a session, entitled “Progress in Intravital Tumor Imaging”, at the 2008 Gordon Conference on Lasers in Medicine and Biology.

### **Conclusion**

Overall we are behind schedule on one task (8), are slightly behind schedule on two tasks (1 and 2), are slightly ahead of schedule on three tasks (4-6), are ahead of schedule on one task (3) and have completed two tasks (7 and 9). These facts, along with the accelerating pace of publications and invited lectures suggests that we are making significant progress, progress that has been enabled by the generous support of the Era of Hope Scholar Award.

# Second harmonic properties of tumor collagen: determining the structural relationship between reactive stroma and healthy stroma.

Xiaoxing Han<sup>1</sup>, Ryan M. Burke<sup>2</sup>, Martha L. Zettel<sup>3</sup>, Ping Tang<sup>4</sup>, and Edward B. Brown<sup>2\*</sup>

<sup>1</sup>Institute of Optics, <sup>2</sup>Department of Biomedical Engineering, <sup>3</sup>Department of Neurobiology and Anatomy, and <sup>4</sup>Department of Pathology. <sup>1,2</sup>Goergen Hall Box 270168, University of Rochester, Rochester, NY, 14627, USA

\* Corresponding Author: [edward\\_brown@urmc.rochester.edu](mailto:edward_brown@urmc.rochester.edu)

**Abstract:** We utilize the polarization and directionality of light emitted by fibrillar collagen via second harmonic generation to determine structural relationships between collagen in mouse mammary tumor models and the healthy mammary fat pad. In spite of the aberrations in collagen production and degradation that are the hallmarks of tumor stroma, we find that the characteristic angle of SHG scatterers within collagen fibrils, and the spatial extent over which they are appropriately ordered for SHG production, are the same in tumor and healthy collagen. This suggests that the SHG-producing subpopulation of collagen is unaffected by the altered collagen synthesis of the tumor stroma, and protected from its aberrant degradative environment.

© 2008 Optical Society of America

**OCIS codes:** (170.0170) Medical Optics and Biotechnology; (180.0180) Microscopy

---

## References and links

1. R. Kalluri and M. Zeisberg, "Fibroblasts in cancer," *Nat. Rev. Cancer*, **6**, 392-401 (2006).
2. M.P. Shekhar, R. Pauley, and G. Heppner, "Host microenvironment in breast cancer development: extracellular matrix-stromal cell contribution to neoplastic phenotype of epithelial cells in the breast," *Breast Cancer Res.* **5** 130-5 (2003).
3. S.Z. Haslam and T.L. Woodward, "Host microenvironment in breast cancer development: epithelial-cell-stromal-cell interactions and steroid hormone action in normal and cancerous mammary gland," *Breast Cancer Res.* **5**, 208-15 (2003).
4. T. Hasebe, et al., "Prognostic significance of fibrotic focus in invasive ductal carcinoma of the breast: a prospective observational study," *Mod. Pathol.* **15**, 502-16 (2002).
5. A. Jukkola, et al., "Postoperative PINP in serum reflects metastatic potential and poor survival in node-positive breast cancer," *Anticancer Res.* **21**, 2873-6 (2001).
6. B.V. Jensen, et al., "Extracellular matrix building marked by the N-terminal propeptide of procollagen type I reflect aggressiveness of recurrent breast cancer," *Int. J. Cancer* **98**, 582-9 (2002).
7. R. Kesikuru, et al., "Elevated preoperative serum ICTP is a prognostic factor for overall and disease-free survival in breast cancer," *Oncol. Rep.* **9**, 1323-7 (2002).
8. Y. Guo, et al., "Subsurface tumor progression investigated by noninvasive optical second harmonic tomography," *Proc Natl Acad Sci U. S. A.* **96**, 10854-6 (1999).
9. P. Wilder-Smith, et al., "Noninvasive imaging of oral premalignancy and malignancy," *J. Biomed. Opt.* **10**, 051601 (2005).
10. S.J. Lin, et al., "Discrimination of basal cell carcinoma from normal dermal stroma by quantitative multiphoton imaging," *Opt. Lett.* **31**, 2756-8 (2006).
11. P.P. Provenzano, et al., "Collagen reorganization at the tumor-stromal interface facilitates local invasion," *BMC Med.* **4**, 38 (2006).
12. E. Brown, et al., "Dynamic imaging of collagen and its modulation in tumors in vivo using second-harmonic generation," *Nat. Med.* **9**, 796-800 (2003).
13. W. Wang, et al., "Single cell behavior in metastatic primary mammary tumors correlated with gene expression patterns revealed by molecular profiling," *Cancer Res.* **62**, 6278-88 (2002).
14. S.V. Plotnikov, et al., "Characterization of the myosin-based source for second-harmonic generation from muscle sarcomeres," *Biophys J.* **90**, 693-703 (2006).



15. H.F. Dvorak, "Tumors: wounds that do not heal. Similarities between tumor stroma generation and wound healing," *N. Engl. J. Med.* **315**, 1650-9 (1986).
16. S. Kaupila, et al., "Aberrant type I and type III collagen gene expression in human breast cancer in vivo". *J. Pathol.* **186**, 262-8 (1998).
17. G.J. Cameron, et al., "Structure of type I and type III heterotypic collagen fibrils: an X-ray diffraction study," *J. Struct. Biol.* **137**, 15-22 (2002).
18. R.M. Williams, W.R. Zipfel, and W.W. Webb, "Interpreting second-harmonic generation images of collagen I fibrils," *Biophys. J.* **88**, 1377-86 (2005).
19. J. Mertz and L. Moreaux, "Second-harmonic generation by focused excitation of inhomogeneously distributed scatterers," *Opt. Commun.* **196**, 325-330 (2001).
20. M.J. Duffy, et al., "Metalloproteinases: role in breast carcinogenesis, invasion and metastasis," *Breast Cancer Res.* **2**, 252-7 (2000).
21. Y. Chen, et al., "DNA vaccines encoding full-length or truncated Neu induce protective immunity against Neu-expressing mammary tumors," *Cancer Res.* **58**, 1965-71 (1998).
22. C.J. Aslakson and F.R. Miller, "Selective events in the metastatic process defined by analysis of the sequential dissemination of subpopulations of a mouse mammary tumor," *Cancer Res.* **52**, 1399-405 (1992).
23. P. Stoller, et al., "Polarization-modulated second harmonic generation in collagen," *Biophys. J.* **82**, 3330-42 (2002).
24. I. Freund, M. Deutsch, and A. Sprecher, "Connective tissue polarity. Optical second-harmonic microscopy, crossed-beam summation, and small-angle scattering in rat-tail tendon". *Biophys. J.* **50**, 693-712 (1986).
25. C.C. Reed and R.V. Iozzo, "The role of decorin in collagen fibrillogenesis and skin homeostasis," *Glycoconj J.* **19**, 249-55 (2002).
26. A.S. Kamoun-Goldrat and M.F. Le Merrer, "Animal models of osteogenesis imperfecta and related syndromes," *J. Bone Miner. Metab.* **25**, 211-8 (2007).

---

## 1. Introduction

The tumor stroma consists of the non-malignant cells in a tumor, the basement membrane, and the extracellular matrix (ECM), and is known to play a significant role in tumor growth [1]. Phenotypic alterations in stromal cells surrounding the malignant cancer cells, especially fibroblasts, contribute to tumor progression [2]. These in turn modify the production and degradation of components of the ECM, resulting in a "reactive stroma" that is a hallmark of the neoplastic transformation [1, 2] (See Fig. 1). This occurs primarily through the increased synthesis and deposition of ECM molecules such as type-I collagen, as well as the degradation of these molecules via elevated synthesis of ECM-degrading proteases (e.g. the matrix metalloproteinases, or MMPs) [1]. This highly altered ECM in turn is believed to play an active role in tumor progression and is known to affect tumor cell migration, to modify the availability of growth factors, and to directly signal tumor cells through integrins [1-3]. As a result the character of the tumor ECM is a highly useful prognostic factor: In pathology practice, breast carcinomas are graded based on the structure and density of ECM staining, while the presence of fibrotic foci in invasive ductal carcinoma of the breast indicates poor prognosis [4]. Furthermore, elevated serum markers of collagen synthesis [5, 6] and degradation [7] are indicators of breast cancer aggressiveness and poor patient survival.

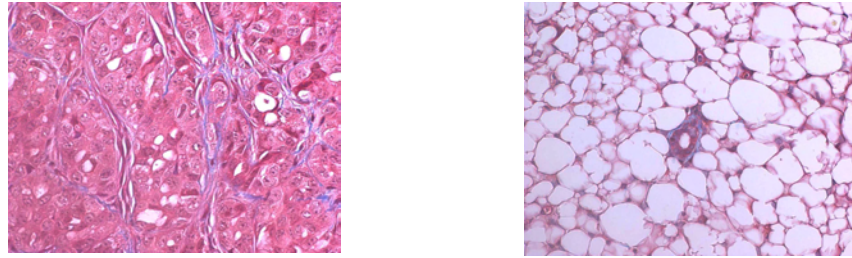


Fig. 1. Enhanced stromal deposition characteristic of many tumors. Masson's Trichrome staining of TG1-1 tumor cells grown in the mammary fat pad of FVB mice (left) as well as the healthy mammary fat pad of FVB mice (right). Abundant bands of ECM, primarily collagen, are evident throughout the tumor tissue as a blue staining (left), and are largely confined to isolated ducts in the healthy mammary fat pad (blue ring in center of right image). Images are 600  $\mu\text{m}$  across.

The central role that the reactive stroma plays in tumor growth, progression, and metastasis means that there is a significant interest in understanding the reactive stroma itself, as well as the relationship between normal stroma and reactive tumor stroma [1]. Second harmonic generation (SHG) has proven to be a useful window into the amount and organization of fibrillar collagen in biological tissues due to its relative specificity and the fact that it is an intrinsic signal. Recently SHG has begun to offer important insight into the reactive stroma of the living tumor: Experimentally-induced and naturally occurring carcinomas have been detected as an alteration in overall SHG intensity [8-11], and that intensity has been shown to scale with overall collagen content [12]. SHG imaging of collagen fibrils has provided insight into the metastatic pattern of malignant cells [11, 13], and revealed the dynamic evolution of collagen content and fibril morphology during tumor growth and treatment [12].

These reports utilized SHG intensity information to reveal the overall morphology of tumor collagen fibrils (location, orientation, and length), and to provide a diagnostic ability to detect malignancy (via scoring of morphology or of average intensity). However, the coherent nature of SHG means that it provides a great deal more information about the structure of the collagen fibrils than is contained simply in its intensity, and hence may reveal important information about the underlying biology of the reactive stroma.

The relationship between incoming laser polarization, outgoing SHG polarization, and macromolecular orientation, reveals the orientation angle of the individual SHG scatterers with respect to the global macromolecule axis [14]. Consequently SHG polarization can be used to provide details of the angular orientation of individual collagen triple helices as they are assembled into collagen fibrils, with single fibril resolution. This is interesting because the reactive stroma of the tumor consists of abnormal proportions of matrix molecules such as collagen I, III, fibrin, and fibronectin [1, 15, 16], and alterations in these ratios, such as that of collagen I to collagen III, are known to alter the angular distribution of triple helices in the overall collagen fibril [17]. These differences in the molecular constituents of healthy versus tumor stromas predict a possible difference in the angular orientation in the individual triple helices.

The relationship between the forward-scattered (F) and backward-scattered (B) SHG signal provides information about the length scale over which the scatterers are appropriately ordered (i.e. SHG-producing) along the laser axis [18, 19]. Therefore this F/B ratio can be used to estimate the overall spatial distribution of appropriately ordered triple helices within collagen fibrils. This is interesting because the reactive tumor stroma is typified by an altered collagen degradation machinery, with elevations of various collagen degrading enzymes such

as the MMPs [1, 20]. These upregulated degradation mechanisms predict a possible difference in the spatial distribution of ordered scatterers in individual tumor collagen fibrils.

In this paper we will specifically utilize the polarization properties of SHG as well as the scattering directionality to explore the relationship between reactive and healthy stroma. We will investigate these optical properties in collagen in two murine breast tumor models, both grown in the mammary fat pad of the mouse, and compare them to collagen from the healthy mammary fat pad in the same mouse strain. The models we will study are the TG1-1 murine mammary tumor cell line which arose spontaneously in a FVB/N *neu*-transgenic mouse [21], as well as the 4T1 murine mammary adenocarcinoma cell line, which arose spontaneously in the BALB strain [22]. Both tumor models exhibit enhanced collagen deposition characteristic of a tumor reactive stroma (see Fig. 2).

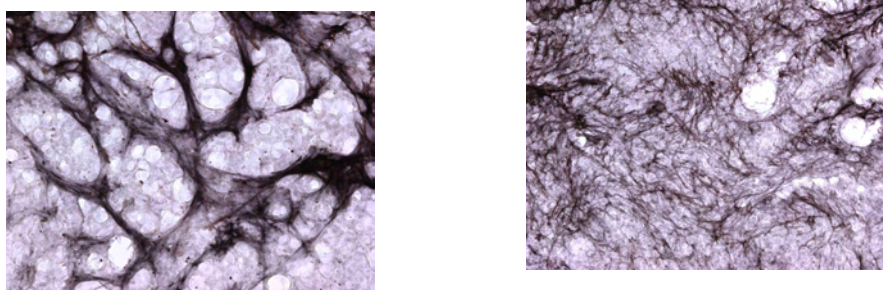


Fig. 2. Anti-Collagen I antibody staining of TG1-1 (left) and 4T1 (right) tumor sections, with DAB contrast. Both tumor types show the enhanced ECM deposition characteristic of tumor reactive stroma, evidenced by enhanced dark brown contrast around “islands” of lightly stained tumor cells. Left image is 600  $\mu$ m across, right is 1.2 mm.

## 2. Experimental methods

### 2.1 Apparatus

The general experimental apparatus is shown in Fig. 3. SHG signal was generated by a Spectra Physics MaiTai Ti:Sapphire laser providing 100 fs pulses at 80 MHz and 810 nm. Beam scanning and image acquisition were performed with an Olympus Fluoview FV300 scanning system interfaced with an Olympus BX61WI upright microscope. The focusing objectives are two identical Olympus UMPLFL20XW water immersion lenses (20 $\times$ , 0.5 N.A.). Objective 1 was used to focus the excitation beam on the sample and at the same time collect the backscattered SHG signal. The backscattered SHG signal was then separated from the excitation beam by a dichroic mirror (Chroma 670 DCSX) and a band pass filter centered at 405 nm (Chroma HQ405/30m-2P) placed after the objective back aperture, and detected by a photomultiplier tube (HC125-02, Hamamatsu). The forward propagating SHG signal was collected by the second objective, reflected by a silver mirror and passed through two filters before being detected by the second PMT. Filter 2 is a short pass filter (Chroma E700SP-2P) that is used to block the 810 nm excitation beam. Filter 3 is a band pass filter centered at 405 nm (Chroma HQ405/30m-2P).

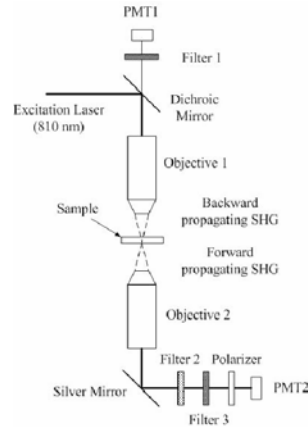


Fig. 3. Experimental Apparatus.

### 2.2a Sample preparation: cell culture

TG1-1 murine mammary tumor cells (courtesy of E. L. Steele Laboratory, Cambridge, MA) and 4T1 murine mammary adenocarcinoma (American Type Culture Collection, Manassas, VA) were grown in T-75 tissue culture flasks (Corning, Corning, NY) containing DMEM supplemented with 4.0 g/L glucose, 10% fetal calf serum (FCS), and 1% penicillin/streptavidin (Invitrogen, Carlsbad, CA). Cells were grown to 90% confluence and harvested with 0.25% trypsin/EDTA (Invitrogen). The trypsin reaction was stopped by adding DMEM containing 10% FCS. Cells were washed three times in sterile Dulbecco's phosphate buffered saline (DPBS: Invitrogen) by centrifuging at 200xg for 10 minutes at 4°C. After the final wash, cells were resuspended in sterile DPBS and kept on ice until injection.

### 2.2b Sample preparation: animal husbandry

All animal techniques were developed and practiced in accordance with the policies of the University Committee on Animal Resources. Female FVB/NJ or BALB/c mice (Jackson Labs, Bar Harbor, ME) at 8 weeks old were anesthetized intraperitoneally with 90 mg ketamine hydrochloride and 9 mg xylazine (Hospira, Lake Forest, IL) per kg body weight. Hair was removed from the ventral surface by use of a depilatory agent. Concentrated tumor cell suspension was injected into the inguinal mammary glands of each animal (a total of 4 injections per animal) at 0.05 mL per injection site. Tumors were allowed to grow to 0.5 cm before being resected from the animal. To ensure maximal variance across animals, only one tumor was taken from each animal for imaging purposes. Mammary fat pads (MFPs) were resected from animals which did not undergo tumor implantation. Female Wistar rats at 1 year old were anesthetized intraperitoneally with 90 mg ketamine hydrochloride and 9 mg xylazine (Hospira, Lake Forest, IL) per kg body weight and sacrificed. Tails were cut into ~1 cm discs with a razor blade and collagenous tendon was teased out onto a coverslip with tweezers.

### 2.2c. Sample preparation: tissue sectioning for SHG imaging

Excised tissues for SHG imaging were sliced into ~100  $\mu$ m sections on a freezing microtome, then mounted in saline between two 150  $\mu$ m coverslips (VWR International, West Chester, PA).

### 2.2 d. Sample preparation: staining.

For Masson's Trichrome staining, samples were excised from the animal and fixed in 10% formalin, then embedded in paraffin and cut into 5  $\mu$ m sections on a vibrating microtome. The resultant sections were mounted on glass slides and stained with Masson's Trichrome. For

anti-collagen I antibody staining, tissue was removed, fixed in buffered (pH 7.4) 4% paraformaldehyde, cryoprotected in 10 and 30% sucrose, and cut at 30  $\mu\text{m}$  on a cryostat. Free floating sections were incubated in a 1:200 dilution of a rabbit polyclonal antibody against Collagen 1 protein isolated from rabbit (AbCam 21286, Cambridge, MA). An anti-rabbit Vector peroxidase kit (Vecotr Laboratories, Burlingame, CA) was used to complete the reaction, and the reaction product was intensified with nickel sulfate.

### 2.2 e. Sample preparation: Electron Microscopy.

Mouse normal mammary gland and tumor specimens were fixed overnight at 4°C in 0.1M phosphate buffered 2.5% glutaraldehyde, postfixed in phosphate buffered 1.0% osmium peroxide for 60 minutes, and dehydrated in a graded series of ethanol to 100 %. The samples were then transitioned to propylene oxide, infiltrated with EPON/Araldite resin, embedded in fresh resin and polymerized for two days at 70°C. One micron sections were cut from epoxy tissue blocks onto glass slides and stained with a 1.0% Toluidine Blue stain to find the appropriate areas to examine ultrastructurally. Thin sections were cut with a diamond knife at 70nm and placed onto 200 mesh copper grids which were sequentially stained with 2.0% aqueous uranyl acetate and lead citrate. The grids were examined using a Hitachi 7100 transmission electron microscope and digital images were captured using a Megaview III digital camera with “AnalySIS” (Soft Imaging Systems, Lakewood, California) software.

### 2.3a Polarization analysis: equipment

For polarization analysis, excitation polarization was fixed parallel to the dichroic mirror surface to avoid elliptical polarizing effects of the primary beamsplitter. This was necessitated by the observation that 810 nm light of >500:1 polarization was degraded to as low as 45:1 upon reflection from the primary dichroic at a polarization angle of 45 degrees, while it maintained a polarization of 250:1 if the polarization angle was fixed parallel to the dichroic surface. The forward-scattered SHG signal was collected with Objective 2 (see Fig. 3), and a polarization analyzer consisting of a cube beam splitter (GL10-A, Newport, Irvine, CA) on a rotary stage was placed directly in front of the PMT.

### 2.3b Polarization analysis: theory

An incoming excitation beam with electric field vector  $\vec{E}$  will induce polarization  $\vec{P}$  in the fibril given by:

$$\vec{P} = \chi^{(1)} * \vec{E} + \chi^{(2)} * \vec{E} * \vec{E} + \chi^{(3)} * \vec{E} * \vec{E} * \vec{E} \quad (1)$$

In the case of second harmonic generation from a system with cylindrical symmetry (such as the collagen fibril), the second term is relevant, and simplifies to [23]:

$$\vec{P} = a\hat{s}(\hat{s} \cdot \vec{E})^2 + b\hat{s}(\vec{E} \cdot \vec{E}) + c\vec{E}(\hat{s} \cdot \vec{E}) \quad (2)$$

where  $\hat{s}$  is the direction of collagen orientation and the coefficients a, b, and c are related to elements of the second-order nonlinear susceptibility tensor  $\chi^{(2)}$ . If the resultant SHG signal is detected through a polarizer oriented at a direction  $\hat{e}$ , the detected SHG intensity is  $I_e \propto (\vec{P} \cdot \hat{e})^2$ . This is given by

$$I_e \propto (\vec{P} \cdot \hat{e})^2 \propto [a \cos \alpha \cos^2 \varphi + b \cos \alpha + c \cos(\alpha - \varphi) \cos \varphi]^2 \quad (3)$$

Where  $\alpha$  is the angle between the collagen fibril and the polarizer axis and  $\varphi$  is the angle between the fibril and excitation beam polarization. Note that this assumes that the fibril is perpendicular to the optical axis. If we consider a z-directed excitation beam interacting with a y-aligned fibril then when  $\alpha=0$ :

$$I_y \propto [(a+c)\cos^2 \varphi + b]^2 \quad (4)$$

and when  $\alpha = \frac{\pi}{2}$ :

$$I_x \propto \left[ \frac{c}{2} \sin 2\varphi \right]^2 \quad (5)$$

Therefore:

$$\frac{I_y}{I_x} = \frac{[(a+c)\cos^2 \varphi + b]^2}{\left[ \frac{c}{2} \sin(2\varphi) \right]^2} \quad (6)$$

If the collagen molecule is considered to be a cylindrically symmetric collection of single-axis scatterers (i.e. elements of the individual triple helices that assemble into a collagen fibril) with a constant polar angle  $\theta$  and a random azimuthal angle  $\phi$ , there are only two independent elements of  $\chi^{(2)}$ , the nonlinear susceptibility tensor, with the result that [14]:

$$\begin{aligned} a &= n - 3m \\ c &= 2b = 2m \\ n &= \chi_{zzz}^{(2)} = N \cos^3 \theta \beta \\ m &= \chi_{zxx}^{(2)} = \chi_{xxz}^{(2)} = N / 2 \cos \theta \sin^2 \theta \beta \end{aligned} \quad (7)$$

Where  $\beta$  is the hyperpolarizability of the individual single-axis scatterers, of density N. This simplification assumes that the susceptibility tensor has Kleinman symmetry regardless of whether the excitation energy is significantly off-resonance [14].

In this case, Eq. (6) becomes:

$$\tan^2 \theta = \frac{2 \cos^2 \varphi}{\sqrt{\frac{I_y}{I_x} \sin(2\varphi) - \sin^2(\varphi)}} \quad (8)$$

And a measurement of  $I_y$  and  $I_x$  at a known  $\varphi$  allow the deduction of  $\theta$ , the polar angle of the SHG scatterers within a given fibril. Note that in Williams et al. [18],

$$\begin{aligned} I_y(\varphi) &= I_p [\rho \cos^2 \varphi + \sin^2 \varphi]^2 \\ I_x(\varphi) &= I_p [\sin 2\varphi]^2 \end{aligned} \quad (9)$$

Where  $I_p$  is the total intensity measured with a perpendicularly polarized illumination beam and the fitting parameter  $\rho$  is used as a measure of the axial polarizing effects of the fibril. Hence:

$$\tan^2 \theta = 2 / \rho \quad (10)$$

And we see that the  $\rho$  term of Williams et al and others [18, 23, 24] is also equivalent to a measurement of  $\theta$ , the polar angle of the SHG scatterers in a given fibril.

We measured  $\theta$  in 100  $\mu\text{m}$  thick acute tissue slices mounted in saline between two coverslips. Each sample was imaged 36 times on an MPLSM with an excitation beam of fixed polarization angle, with each of the 36 images made through an analyzer rotated in 10 degree increments. With that data set, individual fibrils of arbitrary orientation can then be selected, and their intensity versus  $\alpha$  can be plotted as in Fig. 4 by drawing a narrow region of interest around the fibril. The chosen fibril's angle  $\phi$  with respect to the excitation polarization direction can be manually measured from one image using ImageJ (Freeware website), and  $I_x$  and  $I_y$  can then be extracted from the radar plot. Note that absence of photodamage can (and should) be verified by ensuring that  $I(0)=I(360)$ , as shown in Fig. 4.

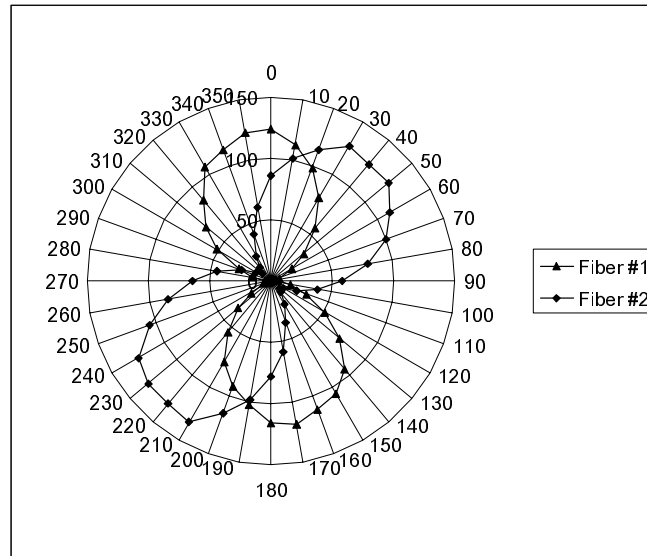


Fig. 4. Radar plot of detected intensity versus analyzer angle. This represents the intensity versus analyzer angle for each of five selected fibrils. In combination with the measured angle of the fibril relative to the laser polarization (vertical in the above graph),  $I_x$ ,  $I_y$ , and hence  $\theta$  can be extracted from this data for each fibril.

#### 2.4 Forwards/Backwards Scattering Analysis

Using the apparatus described in Fig. 3, we measured the detected forward-directed and backward-directed SHG signal in 100  $\mu\text{m}$  thick acute tissue slices mounted in saline between two coverslips. In order to derive the true F/B ratio from these measurements, the effects of scattering as SHG light transits the tissue as well as the relative efficiencies of the two detection pathways must be accounted for. In the manner of Williams et al [18], we applied a dilute solution of 10  $\mu\text{m}$  diameter blue fluorescent polystyrene beads (10m365415, Invitrogen) to the surface of our sample, and F/B ratio images were normalized such that the F/B ratio of in-focus beads was set equal to the ratio measured on the same day in beads in saline between two coverslips [18]. During each imaging session, these images were further

corrected for relative detector inefficiencies by replacing the matched 405/30 SHG filters with matched 535/30 filters, and the F/B ratio of free FITC was measured and normalized to one.

To quantify F/B images, the background signal was first subtracted from the individual forward and backward images, then the F/B ratio of all pixels was calculated. In regions of the original F or B images where there was no significant collagen SHG the F/B ratio fluctuates due to small variations in background noise around a pixel count of zero, and lacks physical meaning. Consequently, an intensity threshold was chosen based upon the B image, producing a binary image mask which set the background pixels to zero and the foreground (e.g. collagen) pixels to one. This mask was multiplied by the F/B image, setting the varying background pixels to zero. Image J was then used to calculate the average pixel count of the resultant masked F/B image, and this was divided by the average pixel count of the binary mask image, producing the average F/B ratio of all pixels within fibrils (i.e. all pixels above threshold in the original B image).

To quantify F/B ratio versus apparent fibril diameter, a blinded observer analyzed 24 fibrils in four tumor samples and 24 fibrils in four mammary fat pad samples by drawing a line transverse to the fibril in ImageJ and fitting the intensity profile along that line to a Gaussian. The  $e^{-2}$  diameter of the fit is then reported as the apparent fibril diameter. A small ROI was also drawn within the imaged fibril at the same location to quantify the average F/B value. The spatial resolution of our system ( $e^{-2}$  radius of the PSF, 0.5 NA lens overfilled with 810 nm excitation light) is 670 nm, so this analysis was limited to those fibrils with an apparent  $e^{-2}$  diameter of 1.0  $\mu\text{m}$  or greater. The PSF will certainly affect the measurement of the diameter of these fibrils over these length scales, but without *a priori* knowledge of the “true” radial spatial distribution of SHG scatterers in the fibril (i.e. solid rod versus hollow cylinder, etc.), we chose not to perform any deconvolution calculation and present the raw data with the independent variable labeled as “apparent” fibril diameter. The resultant scientific conclusion, that there is no statistically significant relationship between F/B ratio and apparent fibril diameter, will be reinforced by any deconvolution calculation as this will serve to stretch the independent variable in Fig. 7 (see below) and render the F/B distribution even flatter.

### 2.5 Fibril orientation.

In a complex three-dimensional network such as the tumor extracellular matrix, the orientation of the individual fibrils relative to the laser axis can vary considerably. If the laser is propagating along the z axis, the fibril orientation relative to the x and y axes can be easily determined by image inspection, but orientation relative to the z axis (i.e. how closely the fibril lies in the plane of the image) will also affect the results of these measurements and must be evaluated. In our F/B measurements, the thresholding step described in section 2.4 above serves to eliminate pixels from fibrils that are oriented at a significant angle out of the plane of the image (i.e. less perpendicular to the z axis), as they are less intense in the SHG images that produce the mask. Manual analysis of the visible fibrils remaining after the masking step reveals that the average length of fibrils analyzed for F/B ratio was  $102 \pm 21 \mu\text{m}$  and  $153 \pm 25 \mu\text{m}$  in the TG1-1 and FVB MFP samples respectively (91 and 96 fibrils in N=4 animals), and  $116 \pm 26 \mu\text{m}$  and  $170 \pm 14 \mu\text{m}$  in the 4T1 and BALB MFP samples respectively (110 and 102 fibrils in N=5 animals). If we model individual fibrils as straight segments diving through the image plane, with an image plane thickness of  $\sim 12$  microns ( $e^{-2}$  z diameter of the PSF), then a visible fibril length of 100 microns corresponds to an angular deviation relative to the plane of  $\tan(\alpha) = 12/100$ , and  $\alpha \sim 7$  degrees. This suggests that the fibrils analyzed were not oriented at significant angles out of the plane of the image, and can be considered perpendicular to the optical axis. The SHG polarization analysis was performed with manually selected fibrils, and for this reason we chose fibrils for analysis with a minimum visible length of 100  $\mu\text{m}$ .



## 2.5 Statistical analysis

Unless stated otherwise, all judgments of statistical significance are based upon the Student's T Test with a threshold for significance of  $p < 0.05$ .

## 3. Results

### 3.1 Comparison of polarization properties of collagen fibrils in tumor and normal mammary fat pad tissue

The relationship between incoming laser polarization, outgoing SHG polarization, and macromolecular orientation, reveals the orientation angle of the individual SHG scatterers with respect to the global macromolecule axis [14]. Using the polarization analysis method described above we found that  $\theta$ , the angle of the elemental SHG scatterers relative to the fibril axis, is  $51.43 \pm 0.91$  degrees ( $N=4$  tumors with six measurements of  $\theta$  per tumor) in TG1-1 tumor collagen and is  $50.61 \pm 1.3$  degrees ( $N=4$  fat pads with six measurements of  $\theta$  per pad) in healthy FVB MFP. These two populations are not statistically significantly different ( $p > 0.05$ ). Likewise  $\theta$  is  $51.78 \pm 4.0$  degrees ( $N=5$  tumors with 11 measurements of  $\theta$  per tumor) in 4T1 tumor collagen and is  $51.71 \pm 4.5$  degrees ( $N=5$  fat pads with 11 measurements of  $\theta$  per pad) in healthy BALB MFP, also not statistically significantly different ( $p > 0.05$ ), and neither is statistically significantly different from TG1-1 nor FVB MFP. This is surprising because the tumor reactive stroma is characterized by alterations in synthesis of collagen I, collagen III, as well as other ECM constituents [1, 15, 16], and the ratio of different collagen components (e.g. collagen I/III ratios [17]) are known to modify the angular assembly of triple helices into the overall collagen fibril. However, it has already been shown that SHG is generated by an appropriately ordered fibrillar subpopulation of the overall collagen in tumor stroma [12]: the polarization data therefore suggests that the altered collagen synthesis properties typical of the reactive tumor stroma do not influence the angular assembly of the ordered (i.e. SHG-producing) subpopulation of fibrillar collagen.

Our measurements of  $\theta$  for tumor and MFP collagen in mice are in close agreement with lower resolution measurements of  $\rho$  in rat tail collagen [23, 24] ( $\rho \sim 1.2$ - $2.0$ , i.e.  $\theta \sim 49^\circ$ , converted via Eq. (10)) and approximately match the  $45.3^\circ$  pitch angle of the collagen glycine proline helix [14]. Surprisingly, however, they appear to disagree with rat tail collagen measurements of  $\rho = 2.6 \pm 0.2$  (i.e.  $\theta = 41.3 \pm 1.1^\circ$ , converted via Eq. (10)) that had the same single-fibril resolution as our measurements [18]. Therefore we also measured  $\theta$  in rat tail collagen and FVB mouse tail collagen, determining that  $\theta = 42.4 \pm 1.8^\circ$  (12 measurements in  $N=2$  animals) in rat tail collagen and  $\theta = 51.8 \pm 3.5^\circ$  (18 measurements in  $N=5$  animals) in FVB mouse tail collagen. To sample an entirely different organ system we also determined that  $\theta = 53.7 \pm 5.0^\circ$  (25 measurements in  $N=4$  animals) in acute sections of FVB mouse colonic submucosa, an organ chosen for its highly elastic collagen structure. See Fig. 5 for a summary of the results. All measurements in mouse organs are statistically significantly different from our measurements in rat ( $p < 0.05$ ), and are not statistically significantly different from each other ( $p > 0.05$ ).

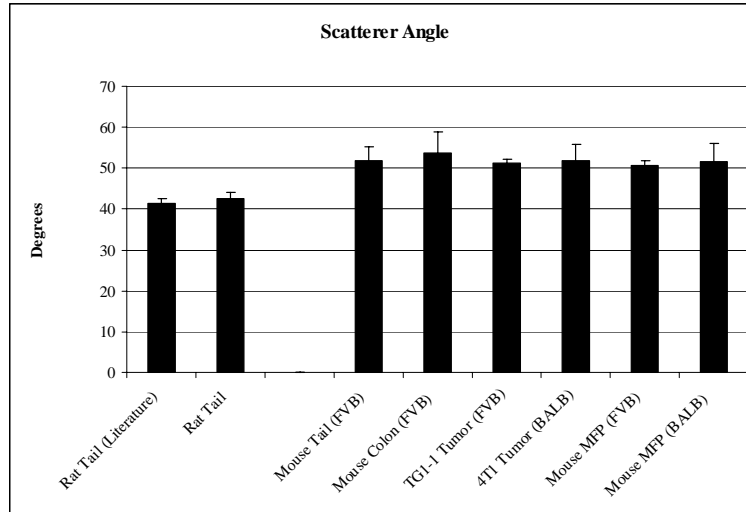


Fig. 5. Measured values of  $\theta$  in rat tail collagen as well as in different organ systems in the mouse. Error bars are standard deviations. All measurements in mouse organs are statistically significantly different from our measurements in rat ( $P < 0.05$ ), and are not statistically significantly different from each other ( $p > 0.05$ ).

Taken together, our results suggest that  $\theta = 42^\circ$  when measured with single fibril resolution in *rat* tail collagen, in agreement with similarly high resolution work done by Williams et al. [18]. However, in *mice*,  $\theta = 51^\circ$  when measured with single fibril resolution in tail, colon, or tumor, in these two different mouse strains. The difference between low- and high-resolution *rat* tail collagen measurements are likely assigned to differences in resolution, as previously suggested [18], and the similarity between our high resolution mouse collagen measurements and low resolution rat collagen measurements is merely coincidence. Overall, our polarization data suggests that not only does the reactive tumor stroma retain an appropriately ordered (i.e. SHG-producing) subpopulation of fibrillar collagen that is assembled in a similar fashion (i.e. with similar  $\theta$ ) to the ordered subpopulation in the mammary fat pad, but that this ordered subpopulation is assembled in a uniform manner *throughout the animal*, while in different species (at least in mice versus rats) the assembly can be altered, producing differing values of  $\theta$ .

### 3.2 Comparison of the forward- and backward-scattering properties of collagen fibrils in tumor and healthy mammary fat pad tissue

The relationship between the forward-scattered and backward-scattered SHG signal provides information about the length scale, along the laser axis, over which the collagen fibril is appropriately ordered to produce SHG. When a highly focused laser beam is used to produce SHG from inhomogeneously distributed ordered scatterers, the forward-scattered to backward-scattered (F/B) ratio approaches 1 as the scatterers' spatial distribution becomes significantly smaller than the excitation wavelength, and rapidly increases as the distribution size approaches the excitation wavelength [19]. Therefore this F/B ratio can be used to estimate the overall spatial distribution of ordered triple helices in collagen fibrils.

We measured the average F/B ratio of the collagen fibrils in 100  $\mu\text{m}$  acute slices of TG1-1 tumor and healthy MFP tissue using the methods described above. Qualitatively, differences in morphology between TG1-1 SHG images and healthy MFP images are readily apparent in the resultant forward-scattered and backward-scattered images (see Fig. 4). In tumor tissue the backward-scattered SHG reveals evident thick bands of collagen, and the SHG within those bands is generally more uniform and homogenous than the forward-scattered image, which

exhibits marked bright fibrils embedded in the bands (i.e. higher individual F/B ratios, see Fig. 6 (a), (b)). In healthy MFP tissue the collagen tends to be arranged in more delicate fibrillar structures (see Fig. 6 (c), (d)), does not share the evident “thick band” organization of the tumor collagen, and is instead more evenly spread across the image. If these images are quantified as discussed above, the average F/B ratio for TG1-1 tumor tissue is  $33.8 \pm 7.7$  (20 quantified images in N=4 animals) and  $34.5 \pm 11.8$  (20 quantified images in N=4 animals) in healthy FVB MFP. There was no statistically significant difference between the two populations ( $p > 0.05$ ). Likewise, the average F/B ratio for 4T1 tumor tissue is  $44.5 \pm 15$  (25 quantified images in N=5 animals) and  $36.3 \pm 17$  (25 quantified images in N=5 animals) in healthy BALB MFP, also not statistically significantly different ( $p > 0.05$ ), and neither is statistically significantly different from TG1-1 nor FVB MFP.

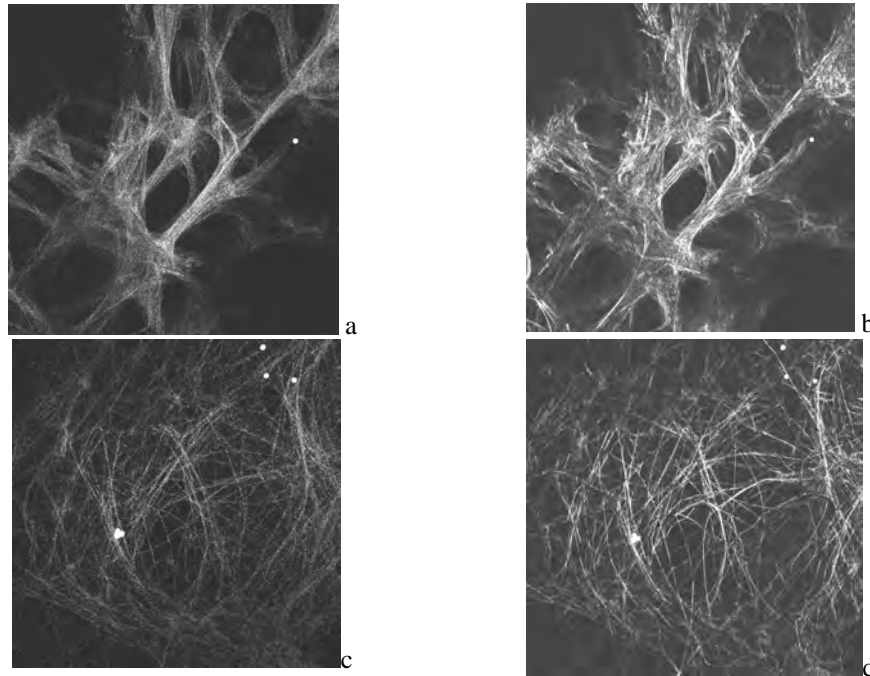


Fig. 6. Top Row: (a) Backward-, and (b) Forward-scattered image of collagen in an acute slice of a TG1-1 mammary adenocarcinoma. Bottom Row: (c) Backward-, and (d) Forward-scattered image of collagen in an acute slice of a healthy FVB mammary fat pad. The small dots in the images are calibration beads. Images are 680 microns across.

Interestingly, the F/B ratio did not vary significantly with the apparent diameter of collagen fibrils in either TG1-1 or FVB MFP (N=3 fibrils in each of 4 tumors and 4 MFPs: see Fig. 7). This F/B ratio analysis of collagen ordering with single fibril resolution has also been performed on rat tail collagen by Williams et al. [18]. They found an F/B ratio of  $\sim 1$ , also independent of fibril diameter (we confirmed those F/B values on our system, producing an F/B ratio for rat tail collagen of  $1.21 \pm 0.14$  (N=5 animals)). Williams et al calculated that an F/B ratio of  $\sim 1$ , independent of fibril diameter, corresponds to collagen fibrils that are appropriately ordered only in a thin shell of  $< 20$  nm thickness, with a center that is not capable of producing SHG due to a defect in collagen ordering [18]. According to the calculations of Mertz et al. [19], an F/B ratio of  $\sim 34$  under 810 nm excitation corresponds to a  $\sim 70$  nm Gaussian distributed cluster of scatterers. Hence we are presented with two possible interpretations of an F/B ratio of  $\sim 34$  that does not vary with fibril diameter: collagen fibrils in murine tumors and in healthy MFP consist of either 1) an SHG-producing shell with a

thickness of  $\sim 70$  nm surrounding a center that is not capable of producing SHG due to a defect in collagen ordering, or 2) a collection of  $\sim 70$  nm diameter rods, appropriately ordered throughout their interior, whose number varies with visible fibril thickness, but whose diameter remains constant. To determine the correct interpretation, we performed Electron Microscopy on TG1-1 and 4T1 tumors, as well as healthy mammary fat pads. We observed that the collagen in each of these samples consisted of multiple rod-like structures with a characteristic diameter on the order of the  $\sim 70$  nm predicted by SHG (see Fig. 8). This suggests that in mouse tumor and mammary fat pad, collagen consists of bundles of  $\sim 70$  nm diameter rods and, unlike the rat tail, this collagen is appropriately ordered throughout the rods and contributes to SHG signal.

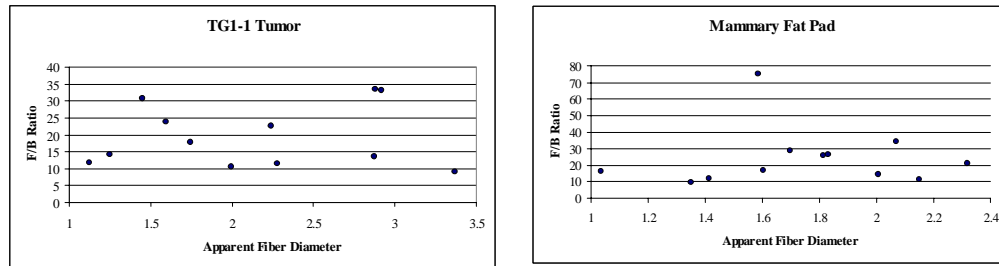
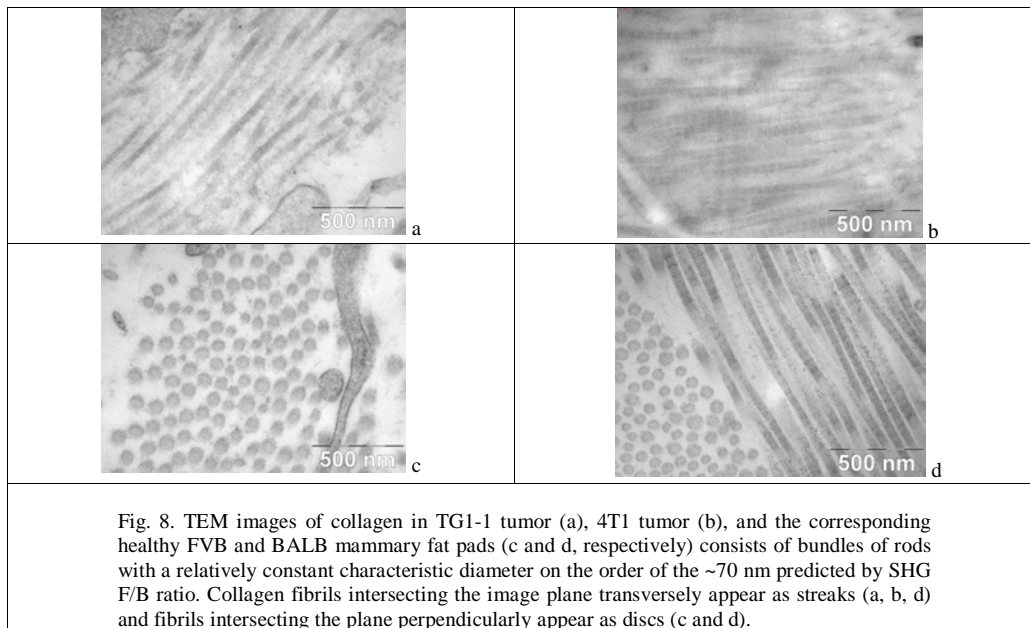


Fig. 7. The F/B ratio does not vary with apparent diameter of collagen fibrils. A fit straight line slope of zero is within the 95% confidence interval. Note that the PSF has an  $e^{-2}$  radius of 0.67  $\mu\text{m}$ . Consequently the stated apparent diameter is a convolution of the Gaussian PSF with the true fibril diameter. However, a deconvolution of the Gaussian PSF with the unknown true distribution (i.e. solid rod, hollow tube, etc.) will rescale the independent variable but will not impart a trend in the data which is not already apparent in the above plots.



The similarity between the average F/B ratio between these mammary tumors and healthy mammary fat pads suggests that the average spatial extent of ordering (along the laser axis, transverse to the fibril axis) is the same. The fact that the F/B ratio is  $\sim 34$  and does not vary significantly with apparent fibril size, combined with the TEM images, suggest the collagen in all of these samples consists of collections of  $\sim 70$  nm rods, appropriately ordered throughout

to produce SHG. These results are somewhat surprising, as the reactive tumor stroma is typified by an altered collagen degradation machinery, with elevations of various MMPs [1, 20], and the SHG-producing collagen in the tumor samples should be accessible to enzymatic degradation (and hence detectable disruption of its ordering). It therefore seems likely that the SHG-generating subpopulation of collagen in tumors is somehow protected from the elevated levels of MMPs that are hallmarks of the reactive stroma [1, 20], perhaps by a coating of molecules such as decorin [25]. Consequently, it seems likely that MMPs in the reactive stroma primarily interact with the subpopulation of collagen which does not produce detectable SHG, and that degradation and synthesis of collagen in that inappropriately ordered subpopulation is the primary cause of the plasma-borne markers of collagen synthesis and degradation which are hallmarks of poor prognosis in breast cancer patients [5-7].

#### **4. Conclusion.**

We have shown that the angle of the SHG scatterers relative to the fibril axis in collagen fibrils in TG1-1 and 4T1 murine mammary tumors is equal to that in fibrils in the healthy mammary fat pad. We have also shown that the spatial distribution of ordered (i.e. SHG-producing) triple helices in collagen fibrils in TG1-1 and 4T1 tumors is equal to that in fibrils in the healthy mammary fat pad. Specifically, the triple helices form ~70 nm diameter rods, with multiple rods clustering together to produce larger diameter fibrils. Unlike collagen in the rat tail, these rods are appropriately ordered for SHG generation throughout their diameter. These observations are somewhat surprising in light of the myriad differences in both collagen synthesis and degradation between the tumor reactive stroma and the healthy mammary fat pad. They suggest that the subpopulation of collagen that is appropriately ordered to produce SHG is a “stable pool” whose location may be altered in tumorigenesis (i.e. collected in bands versus diffusely distributed, as shown in Fig. 6(a) vs 6(c) but whose production mechanism remains unchanged (i.e. similar  $\theta$ ) and which is somehow protected from the altered degradative environment (i.e. similar F/B ratio).

We have also shown that there are fundamental species-specific differences in these two key structural properties of SHG-producing collagen fibrils. In rat tail collagen the angle of SHG scatterers in collagen fibrils is significantly different from that in mouse tail collagen, while this angle remains unchanged between mouse tail, colonic submucosa, mammary fat pad, and mammary tumor tissue (across two different strains of mice). Similarly, the spatial distribution of ordered triple helices within collagen fibrils is significantly different in rat tail collagen versus mouse mammary fat pad while this distribution remains unchanged in mouse mammary tumor tissue (across two different strains). This suggests that these two properties are most significantly altered when the collagen structure itself is altered at the genetic level (i.e. rat genome vs mouse genome) versus alterations in the synthesis rates, ratios of collagen subtypes, or levels of degradation enzymes, such as found in the tumor reactive stroma. Therefore these optical properties may be useful in studying genetic disorders of collagen, such as in Osteogenesis Imperfecta [26].

#### **Acknowledgments**

This work is supported by Department of Defense grant W81XWH-05-1-0396. We thank Drs. Ania Majewska and Dr. Julie Zhang for use of, and assistance with, the vibrotome for tissue sectioning. We also thank Karen Bentley of the University of Rochester Medical Center Electron Microscopy Core Facility for use of, and assistance with, the generation of the electron microscopy images.

# Improved model of fluorescence recovery expands the application of the multi-photon fluorescence recovery after photobleaching technique within the *in vivo* environment

Kelley D. Sullivan\*, William H. Sipprell III<sup>#</sup>, Edward B. Brown Jr.<sup>§</sup>, and Edward B. Brown III<sup>¶</sup>

\*Department of Physics and Astronomy, University of Rochester, Rochester, NY 14627

<sup>#¶</sup>Department of Biomedical Engineering, University of Rochester, Rochester, NY 14642

<sup>§</sup>Department of Physics, Manhattan College, Riverdale, NY 10471

**Keywords:** MP-FRAP; diffusion; convection; flow

**Running title:** MP-FRAP with convective flow

# Abstract

Multi-photon fluorescence recovery after photobleaching (MP-FRAP) is a well-established microscopy technique used to measure the diffusion of macromolecules in biological systems. We have developed an improved model of the fluorescence recovery that includes the effects of convective flows within a system. We demonstrate the validity of this “flow model” in simulations as well as in *in vitro* systems with known flow velocities and diffusion coefficients. We show that this flow model broadens the applicability of the MP-FRAP technique when flows are present by expanding the range of flow velocities over which the diffusion coefficient can be determined accurately, as well as by allowing for simultaneous measurement of the flow velocity over certain regimes. We also demonstrate the effectiveness of the flow model *in vivo* by measuring diffusion and flow within tumor vessels of 4T1 murine mammary adenocarcinomas implanted in the dorsal skinfold chamber.

# Introduction

The fluorescence recovery after photobleaching (FRAP) technique was developed in the 1970’s as a method to probe the local mobility of macromolecules in living tissue (1–4). Briefly, FRAP is performed by using an intense laser flash to irreversibly photobleach a region of interest within a fluorescent sample and then monitoring the region of interest with the attenuated beam as still-fluorescent molecules from outside the region diffuse inward to replace the bleached molecules. FRAP relies on single-photon excitation of the fluorescent sample, which generates fluorescence throughout the light cone of the objective. Fluorescence and photobleaching are therefore unconfined in three dimensions, generally limiting the technique to thin samples ( $\sim 1\ \mu\text{m}$ ) for measurement of absolute diffusion coefficients. FRAP with spatial Fourier analysis (SFA-FRAP) (5) allows thicker samples to be investigated, however, deep-tissue imaging is still prohibited due to the poor depth penetration of epifluorescence microscopy. The intrinsic spatial confinement of multiphoton excitation (6) allows multiphoton fluorescence recovery after photobleaching (MP-FRAP) to be performed within thick samples, while the greater depth penetration of multiphoton imaging (7) allows MP-FRAP to be performed deep within scattering samples.

The existing theory of MP-FRAP does not account for the possibility of convective flow within the focal volume, a situation which is now likely to arise as MP-FRAP is applied to a greater variety of *in vivo* applications. The presence of an unexpected significant convective flow in an MP-FRAP experiment can produce erroneously high diffusion coefficients (see below). It is important, therefore, to include convective flow in the MP-FRAP derivation, and to determine over what range of flows the MP-FRAP technique can thereby provide accurate diffusion coefficients. An additional benefit is that for a relatively wide range of diffusion coefficients and flow velocities, both parameters can be measured accurately by MP-FRAP with the new derivation.

Other techniques have addressed the possibility of combined convective flow and diffusive transport. Conventional (one-photon) FRAP and SFA-FRAP both have the ability to detect directed flows (2, 8). As discussed, however, neither offers the combined spatial resolution and depth penetration of MP-FRAP. Other techniques offering similar spatial resolution

as MP-FRAP include multi-photon fluorescence correlation spectroscopy (MP-FCS) (9, 10) and the closely related two-photon image correlation spectroscopy (ICS) (11). Both of these techniques have the capability to measure flow as well as diffusion, and a relatively new variation of image correlation spectroscopy, k-space ICS (12), explicitly offers the ability to measure diffusion and velocity simultaneously. However, the need of the various correlation spectroscopies for both low concentrations of fluorophores and low background noise, compared to the need of FRAP techniques for high concentrations of fluorophores and subsequent resistance to background noise means that the correlation spectroscopies and the photobleaching recovery techniques are complementary, not competitive.

In this paper we will first derive the theory of MP-FRAP with flow and diffusion. Then we will use simulations to understand how MP-FRAP curves evolve under flow and to predict how the standard and flow MP-FRAP models will fit the data. Next, we will perform MP-FRAP experimentally in situations with known flow velocity using tracers with known diffusion coefficients and determine specific “cutoff velocities” which define where the standard and flow models produce accurate diffusion coefficients (and/or flow velocities). Lastly, we will apply the new flow model *in vivo* in conditions of varying flow.

## Theory

In the standard MP-FRAP model, diffusion is assumed to be the only mechanism for recovery. The diffusive recovery after a brief bleaching pulse is given by Brown et. al (13):

$$F(t) = F_o \sum_{n=0}^{\infty} \frac{(-\beta)^n}{n!} \frac{1}{(1+n+2nt/\tau_D)} \frac{1}{(1+n+2nt/R\tau_D)^{1/2}} \quad (1)$$

where  $\beta$  is the bleach depth parameter,  $\tau_D$  is the characteristic diffusion time, and  $R$  is the square of ratio of the axial and radial dimensions of the focal volume. The diffusion coefficient is given by  $D = \omega_r^2/8\tau_D$ , where  $\omega_r$  is the radial width of the two-photon focal volume. With only two fitting parameters,  $\beta$  and  $\tau_D$ , fits to the fluorescence recovery using the standard model are very robust. In the absence of flow, a three to four decade range of input seed values for the fitting parameters required by the fitting program will produce convergence to the same, low residual, fit.

By adding a time-dependent coordinate shift to the standard model of diffusive recovery before its convolution with the excitation laser profile (see Appendix), we arrive at an improved “flow model” that describes fluorescence recovery in the presence of convective flow as well as diffusion:

$$F(t) = F_o \sum_{n=0}^{\infty} \frac{(-\beta)^n}{n!} \frac{\exp\left[-\frac{4n(t/\tau_v)^2}{1+n+2nt/\tau_D}\right]}{(1+n+2nt/\tau_D)(1+n+2nt/R\tau_D)^{1/2}} \quad (2)$$

In this model, a third fitting parameter,  $\tau_v$ , is introduced, which describes the characteristic recovery time due to linear flow. The flow velocity is easily calculated as  $v = \omega_r/\tau_v$ . This formula produces MP-FRAP recovery curves that are indistinguishable from MP-FRAP recovery curves derived using the original formula (Eq. 1) when flow velocities are extremely



low. Increasing the flow velocity alters the shape of the MP-FRAP recovery curves, eventually producing curves that approach an almost sigmoidal shape at high flow velocities (see Fig. 1).

With this improved model, we can now measure diffusion accurately in the presence of flow while simultaneously measuring the flow velocity. However, the introduction of a third fitting parameter complicates the fit. We might now expect that when either diffusion or velocity dominates the fluorescence recovery, the fitting program will yield inaccurate values for the non-dominant parameter. Care must be taken to define the range of flow velocities over which diffusion and velocity may be measured accurately.

## Methods

### Simulations

Simulated fluorescence recovery curves were generated using the flow model and fit to both the original, or “standard”, MP-FRAP model which does not allow for the possibility of flow and the modified, or “flow”, MP-FRAP model which allows for diffusion and flow using the `lsqcurvefit` function in MATLAB (The MathWorks, Natick, MA). We added Poisson distributed noise to the simulated data in proportion to the signal to noise ratio expected for either *in vitro* (3%) or *in vivo* (10%) experiments as determined from previous experience (13). Three experimentally relevant bleach depths were also chosen: 0.2, 0.6, and 1.0 (13). For each bleach depth/noise combination, a range of diffusion coefficients and flow velocities was explored. After fitting the recovery curves, the ratio of fit diffusion coefficient to input diffusion coefficient (with both the standard and flow model) and the ratio of fit velocity to input velocity (with the flow model) was plotted *versus* input velocity. Initial seed values for the fitting parameters required as inputs to the `lsqcurvefit` function were generated via algorithms developed from limits to the flow model equation and assumed no *a priori* knowledge of the experimental system or of the particular flow velocities and diffusion coefficients. Specifically, the formula used to calculate a seed value for  $\beta$  was derived by solving the recovery equation (Eq. 2) at  $t = 0$  for  $\beta$  in terms of  $F(0)/F_o$ , plotting a range of bleach depth parameters as a function of  $F(0)/F_o$ , and then choosing the best-fit polynomial to the curve. Seed values for  $\tau_D$  are easily estimated as the one half recovery time of the MP-FRAP recovery curve. And the seed value for velocity is approximated as  $v = (x_{1/2})^{1/2}(\omega_r/\tau_{1/2})$ , where  $x_{1/2}$  was determined by taking the limit of the recovery equation as  $\tau_D \rightarrow \infty$ , then plotting  $F(x)/F_o$ , where  $x = (vt/\omega_r)^2$ , and finally picking the value at which  $F(x)/F_o$  was half recovered.

### Experimental apparatus

Laser light was generated by a tunable, mode-locked Ti:Sapphire laser (Mai Tai; Spectra Physics, Mountain View, CA), yielding 80 fs pulses at a repetition rate of 100 MHz. Rapid modulation of the laser power to produce monitor and bleach intensities was provided by a KDP\* Pockels Cell (model 350-80; Conoptics, Danbury, CT). Timing of the bleach and monitor pulses was delivered by a pulse generator (model DG535, Stanford Research Systems,

Sunnyvale, CA), while the voltage output to the Pockels Cell was set and switched via a home made control box. The output of the Pockels Cell was directed through an Olympus Fluoview 300 laser-scanning microscope to the back aperture of the objective lens (0.8 NA, 40x water immersion; Olympus, Center Valley, PA). Proper overfilling of the back aperture of the objective lens was achieved for all experiments (see PSF calibration below). Overfilling is accomplished when the  $1/e$  radius of the laser beam is greater than or equal to the radius of the back aperture of the lens. The objective lens focused the excitation beam within the fluorescent sample (Fig. 2). The fluorescence emission was separated from the excitation by a short pass dichroic mirror (model 670 DCSX-2P, Chroma Technologies, Brattleboro, VT). Emission signals were further separated by a second dichroic mirror, and each was detected by a photomultiplier tube (PMT) (Hamamatsu, Bridgewater, NJ). The output from the PMT monitoring the green channel (FITC) could be directed, via a simple home made switch box, to a photon counter (SR400; Stanford Research Systems, Sunnyvale, CA) for general inquiry into the fluorescence behavior or to a multi-channel scaler/averager (SR430; Stanford Research Systems, Sunnyvale, CA) for fluorescence recovery data collection. Output from the PMT monitoring the red channel (to image fluorescent beads; see below) was directed to the Olympus imaging software. For increased throughput, data collection was largely automated via LabVIEW (National Instruments, Austin, TX).

## PSF calibration

The  $1/e^2$  radial and axial dimensions of the two-photon excitation volume were verified by scanning the excitation volume across sub-resolution fixed fluorescent beads (Molecular Probes, Invitrogen, Carlsbad, CA). For the radial dimension, xy scans were taken and the intensity profiles measured using Image J (NIH, Bethesda, MD). For the axial dimension, z-stack images were acquired, the intensity profile of each image in the stack analyzed in Image J to determine the peak of the intensity profile, then the peak values plotted versus image depth to build the intensity profile in the axial direction. The results of both measurements were compared against theoretical values. For this work, we defined the dimensions of the focal volume to be  $0.403\ \mu\text{m}$  in the radial direction and  $2.22\ \mu\text{m}$  in the axial direction for a 0.8 NA objective, properly overfilled with 780 nm laser light.

## *In vitro* MP-FRAP

For *in vitro* testing of the flow model, fluorescent samples were produced by mixing fluorescein isothiocyanate (FITC) conjugated to bovine serum albumin (BSA) or 2000 kD dextran (Molecular Probes, Invitrogen) diluted to 1 mg/ml in phosphate buffered saline (PBS) with  $1\ \mu\text{l/ml}$  red fluorescent microspheres (FluoSpheres; Molecular Probes, Invitrogen). The solution was suspended in a syringe and allowed to flow freely through a thin tube (0.28 mm radius) and into a channel, capped by a no. 1.5 coverslip and immersed in a pool filled with PBS. The rate of flow was set by adjusting the height of the syringe relative to the channel. For FRAP measurements, the excitation focal volume was parked within the flowing solution in the channel, and the excitation intensity rapidly modulated between a strong bleaching pulse and a weak monitoring pulse. For independent velocity measurements, the excitation volume was multiply scanned along a 1D line parallel to the fluid flow at constant excitation

intensity, thus producing a line-scan image with dimensions of position *versus* time (14). The angle of the sporadic streaks in the line-scan image, representing the movement of the microspheres, was used to calculate the flow velocity.

## Cell/tissue culture and animal husbandry

4T1 murine mammary adenocarcinoma cells (American Type Culture Collection, Manassas, VA) were grown in T-75 tissue culture flasks (Corning, Corning, NY) containing RMPI-1600 supplemented with 4.0 g/L glucose, 10% fetal calf serum, and 1% penicillin/streptavidin for optimal growth (all Invitrogen). Cells were grown to 100% confluence and harvested with 0.25% trypsin/EDTA (Invitrogen), then incubated for ten minutes on ice in calcium/magnesium-free sterile DPBS (Invitrogen).

Female Balb/cByJ mice (Jackson Labs, Bar Harbor, ME) at eight weeks old were anesthetized using a ketamine/xylazine mixture (Hospira, Lake Forest, IL) at 90/9 mg/kg/mouse. Hair was removed from the ventral surface by use of a depilatory agent. Concentrated 4T1 suspension was injected into the inguinal mammary glands of each animal (four injections per animal) at 0.05 mL per injection site. Tumors were allowed to grow to 0.25 cm before being resected from the animal. To ensure that maximal variance across animals was addressed, only one tumor was taken from each animal for imaging purposes.

Male Balb/cByJ mice (Jackson Labs) were similarly anesthetized and outfitted with a titanium dorsal skinfold chamber as previously described (15). A small chunk (no more than 0.5 mm diameter) of resected primary 4T1 tumor was placed in the window and allowed to grow for one week before imaging.

All animal techniques were developed and practiced in accordance with the University of Rochester Committee on Animal Resources policy.

## *In vivo* MP-FRAP

Animals containing tumors growing in the dorsal skinfold chamber were anesthetized using a ketamine/xylazine mixture (Hospira, Lake Forest, IL) at 90/9 mg/kg/mouse. 0.2 ml of a 10 mg/mL solution of 2000 kD dextran was injected intravenously and anesthetized animals were positioned under the microscope objective lens. MP-FRAP was performed as described above, with the focal volume positioned in the center of the vessel in the xy plane, but largely within the cell-free region along the z axis to maximize fluorescent signal. Line-scans were also performed as described, using the “shadows” of RBCs, which do not take up 2000 kD dextran, instead of fluorescent beads.

## Data analysis

As with the simulated data, experimental MP-FRAP data was fit to the standard and flow models using the MATLAB `lsqcurvefit` function, which is based on the Levenberg-Marquardt algorithm. Line-scan data was analyzed using Image J software.

# Results

## *In silico*: Simulations of MP-FRAP with flow

By generating and fitting simulated fluorescence recovery curves, we determined the capabilities of the flow model, compared to those of the standard MP-FRAP model, when flows are present. Limitations to the standard model were assessed by generating fluorescence recovery curves using the flow model and fitting them to the standard model, then comparing the input diffusion coefficients and fit diffusion coefficients. Beginning with a combination of a signal to noise ratio of 3% and a bleach depth parameter of 0.6, we generated curves for a series of diffusion coefficients ranging from 0.5 to 500  $\mu\text{m}^2/\text{s}$  over a range of flow velocities from 0.1 to 10000  $\mu\text{m}/\text{s}$ . Fig. 3 shows that for this series of diffusion coefficients, the standard model begins to yield erroneously high diffusion coefficients as the flow velocity increases, and that the error commences in a flow velocity regime which varies with the diffusion coefficient of the tracer in question. By scaling the velocity along the horizontal axis (inset), such that  $v_s = v(\omega_r/8D)$ , the curves for each value of the diffusion coefficient overlay onto one curve and a universal behavior can be observed: the standard model produces erroneous diffusion coefficients ( $D_{\text{fit}}/D_{\text{input}} \gg 1$ ) as the scaled velocity approaches the range of  $v_s = v(\omega_r/8D) \sim 1$ . This scaling behavior allowed us to complete our investigations of the remaining noise/bleach depth parameter combinations using diffusion coefficients representative of BSA and dextran only, the two tracer molecules used in our *in vitro* experiments. With all combinations of noise and bleach depth evaluated (3% and 10% relative noise, and  $\beta$  of 0.2, 0.6, 1.0), we find that the behavior of the  $D_{\text{fit}}/D_{\text{input}}$  curve is unchanged (data not shown).

To evaluate the expanded capabilities of the flow model, we generated *and* fit fluorescence recovery curves using the flow model for diffusion coefficients representing BSA and dextran over a range of flow velocities. We show representative results in Fig. 4a for  $\beta = 0.6$  and  $S/N = 3\%$ , where the ratio of fit diffusion coefficient to input diffusion coefficient is displayed along with the ratio of fit velocity to input velocity. At the extremes of the plot, representing results from fits to fluorescence recoveries dominated by either diffusion (on the left) or velocity (on the right), the fit accurately determines the dominant parameter (i.e. a ratio of one with a small standard deviation), while poorly determining the non-dominant parameter (i.e. a ratio not equal to one and/or a large standard deviation). For a wide range of scaled velocities, the effects of diffusion and velocity on the fluorescence recovery dynamics are reasonably balanced and both diffusion and velocity are accurately determined. We can define three regimes: 1. diffusion-dominated, in which only the diffusion coefficient is accurately determined; 2. balanced, in which both diffusion and velocity are accurately determined; and 3. velocity-dominated, in which only velocity is accurately determined. After completing investigations of the full collection of bleach depth/noise combinations, we find that the balanced regime, where both diffusion and velocity are well-fit, is narrowed as  $\beta$  decreases and/or the signal to noise ratio increases (Fig. 4b) and is broadened as  $\beta$  increases and/or as the signal to noise ratio decreases (Fig. 4c). We also find that as we move into either of the two regimes where one parameter dominates the other, the standard deviation in the measurement of the non-dominant parameter increases precipitously. This increase in the standard deviation of the non-dominant parameter is more sensitive to the scaled velocity than is the error in the

measurement (error defined as a ratio of  $D_{\text{fit}}/D_{\text{input}}$  or  $v_{\text{fit}}/v_{\text{input}}$  which deviates from one), therefore, the standard deviation is a more conservative indicator of inaccurate results. The arrows in Fig. 4a point to regimes where the standard deviation in the  $D_{\text{fit}}/D_{\text{input}}$  ratio grows significantly, even when the average  $D_{\text{fit}}/D_{\text{input}}$  is itself still close to one. In Fig. 3, however, we see that using the standard model to fit data whose recovery is dominated by flow does not produce large standard deviations because the fitting routine must erroneously assign all of the recovery kinetics to diffusion, thus producing a very precise, but very inaccurate,  $D$ . It is only when the flow model is used to determine  $D$  (and  $v$ ) that the standard deviations can grow large while the error remains relatively small, as the bulk of the recovery is assigned to the dominant parameter and the negligible contribution from the non-dominant parameter can fluctuate.

From these simulations we therefore predict that the error in  $D$  in both the standard and flow model increases with increasing flow velocity, while for some range of low flow velocities both models will produce accurate diffusion coefficients. We also predict that there will be a range of flow parameters where the flow model produces accurate diffusion coefficient *and* flow velocities, and a range of flow parameters where the flow model produces only accurate flow velocities. Further, we predict that, using the flow model, the standard deviation of the non-dominant parameter will increase before the absolute error in the measurement, while the standard model, lacking a non-dominant parameter, will produce very precise, but very inaccurate, values of  $D$  as flow increases.

## ***In vitro* MP-FRAP**

For a direct measure of the capabilities and limitations of the two models, we designed an experimental system with known diffusion and known directed flow. FITC-BSA and FITC-dextran were used as tracer molecules. The dramatic difference in molecular weight, 64 kD and 2000 kD for BSA and dextran, respectively, was necessary to access the widest range of relevant scaled velocities as suggested by the simulations. To determine accuracy of fit, the fit diffusion coefficient was compared against the diffusion coefficient for a diffusion-only system, i.e. performed without experimental flow and fit to the standard MP-FRAP model, and the fit velocity was compared against the velocity obtained from line-scan data taken concurrently with the MP-FRAP measurements. In the literature, diffusion values for BSA vary from 55 to 62  $\mu\text{m}^2/\text{s}$  (5, 16–20), while values for dextran range from 8.4 to 9.1  $\mu\text{m}^2/\text{s}$  (18, 20), when adjusted to 20°C via the Stokes-Einstein relation. Our diffusion-only measurements yielded  $52 \pm 0.7 \mu\text{m}^2/\text{s}$  and  $9.2 \pm 0.05 \mu\text{m}^2/\text{s}$  for BSA and dextran, respectively, consistent with the literature.

The results of our measurements with flow are summarized in Figs. 5 and 6. Fig. 5 compares results of the accuracy of the diffusion coefficient given by both the standard (red) and flow (blue) models for the same collection of data sets. As predicted from our simulations, the standard deviation in the results of the standard model does not increase even when the error becomes great (i.e.  $D_{\text{fit}}/D_o \gg 1$ ). In order to determine a cutoff velocity where the standard model no longer produces an accurate diffusion coefficient, we define an inaccurate fit by the standard model as one in which  $D_{\text{fit}}/D_o$  is statistically significantly greater than 1.2 (determined by a one-sided hypothesis test), and we see that the standard model begins yielding inaccurate fits to the diffusion coefficient at a cutoff value of  $v_s \approx 0.3$ .

The flow model, meanwhile, continues to provide accurate values for the diffusion coefficient for significantly greater flow velocities.

Fig. 6 displays the accuracy of the results for both the diffusion coefficient and the velocity as determined by fitting with the flow model. For the flow model, our simulations have shown that the standard deviation in our measurements of the non-dominant parameter can increase at smaller values of the dominant parameter than does the absolute error in the measurement. We therefore define a poor measurement as having a standard deviation greater than 15% of the mean value. Using this criterion, we can expect the transition from a diffusion-dominated to a balanced recovery to occur at  $v_s \approx 0.2$  and the transition from a balanced to a velocity-dominated recovery to occur at  $v_s \approx 3$ . These experimentally determined cutoff velocities are valid for  $\beta \approx 0.5$  and  $S/N \approx 4\%$ , chosen to match typical experimental values (13). While our simulations have shown that differing amounts of noise and bleach depth will alter these cutoff values slightly (see Fig. 4), we can use these cutoff values as estimates of the range of behaviors expected in our *in vivo* experiments.

## ***In vivo* MP-FRAP**

We chose to measure diffusion and convection within living tumor vessels as an illustrative example of the necessity of using the flow model to determine diffusion coefficients when flows are present, as well as of the added advantage of the flow model to yield accurate flow velocities as flows become significant. Importantly, by continuing to employ the line-scan technique, we can concurrently measure the red blood cell (RBC) velocity, which can be used as an independent *in vivo* measurement of transverse flow to compare with our MP-FRAP velocity measurements. Fig. 7 shows representative recovery curves and associated fits to the flow model for 2000 kD dextran in three different tumor vessels. In each case, a length of vessel was chosen that lay parallel to the plane of imaging. Table 1 shows the results of fitting the curves to both the standard model and the flow model, as well as the average RBC velocity in that part of the vessel. We have also tabulated the value of the predicted flow scaled velocity,  $v_s$ , as calculated from RBC velocities and *in vitro* diffusion coefficient measurements (adjusted to 37°C and  $\eta = 1.2$ , the viscosity of plasma (21), via the Stokes-Einstein relation).

In vessel 1 we see that the RBC velocity was  $14 \pm 3 \mu\text{m/s}$ , producing a predicted scaled velocity of  $0.08 \pm 0.02$ , well below the estimated cutoff velocity for accurate fitting with the standard MP-FRAP model and comfortably within the diffusion dominated regime for the flow model. From this we would predict that both the standard and flow models would yield an accurate value for the diffusion coefficient, while the flow model would provide an inaccurate value for the flow velocity. As predicted, the two techniques produce identical values for the diffusion coefficient,  $D = 9.28 \mu\text{m}^2/\text{s}$ , which is consistent with literature values when adjusted via the Stokes-Einstein relation using an estimated plasma viscosity of  $\eta = 1.2$ . Meanwhile, as predicted, a significant difference is evident between the measured flow velocity,  $v = 0.02 \mu\text{m/s}$ , and the RBC velocity,  $v = 14 \pm 3 \mu\text{m/s}$ .

Vessel 2 has a predicted scaled velocity of  $0.45 \pm 0.05$ , which is above the cutoff velocity for the standard MP-FRAP model but within the balanced regime for the flow model. This indicates that the standard model should overestimate the diffusion coefficient, while the flow model should yield accurate results for both the diffusion coefficient and the flow ve-

locity. As expected, standard MP-FRAP produces an erroneously high diffusion coefficient ( $D = 19.6 \mu\text{m}^2/\text{s}$ ) due to the presence of significant flow. Also as predicted, flow MP-FRAP produces a diffusion coefficient ( $D = 9.68 \mu\text{m}^2/\text{s}$ ) which compares well with the value obtained from vessel 1 and with the extrapolated literature value. This suggests that this measurement is not impacted by the increased flow velocity. Additionally, the flow model yields a result for the flow velocity which is comparable to the RBC velocity. The slight difference between the plasma velocity produced by the flow MP-FRAP model and the RBC velocity produced by the line-scans is statistically significant ( $69.3$  vs  $83 \pm 10 \mu\text{m}/\text{s}$ ,  $P = 0.036$ ). However, on the edge of the cell-free layer in blood vessels it is expected that the RBC velocity will be slightly larger than the plasma velocity (21).

Vessel 3 has a predicted scaled velocity of 6.24, well above the cutoff velocity for standard MP-FRAP and in the velocity dominated regime for the flow model. From this, we expect both the standard and flow models to yield inaccurate results for the diffusion coefficient, while the flow model should continue to provide an accurate measure of the flow velocity. As predicted, standard MP-FRAP produces a diffusion coefficient that is erroneously high ( $D = 250 \mu\text{m}^2/\text{s}!$ ), due to the presence of dominant flow. Flow MP-FRAP also produces an erroneously high diffusion coefficient ( $D = 34.9 \mu\text{m}^2/\text{s}$ ). This suggests that the flow in this vessel is rapid enough produce detectable deviations in diffusion coefficient measurements, even for the flow model. Finally, the plasma velocity determined by the flow MP-FRAP model is comparable to the RBC velocity, although the small difference between the measured flow velocity and the RBC velocity is statistically significant ( $987$  vs  $1139 \pm 80 \mu\text{m}/\text{s}$ ,  $P = 0.013$ ). This small difference is again anticipated in tumor vessels, and allows us to conclude that the fit velocity value is accurate.

## Discussion

MP-FRAP is a well-established technique for measuring the diffusion of macromolecules within biological systems. However, the presence of unanticipated convective flow can produce erroneous diffusion coefficients. Here we have derived a new model for fitting MP-FRAP recovery curves, which improves upon the standard MP-FRAP recovery model by including the effect of convective flow. We have evaluated this new model in simulations and *in vitro* experiments with known flows and known diffusion coefficients as a means of exploring the advantages of the flow model compared with the standard model and also of testing the computational limitations of fits to the flow model. We have also demonstrated the new MP-FRAP equations in measurements of diffusion and velocity *in vivo* within tumor blood vessels, whose RBC velocities provide a known velocity with which to compare our results.

### Standard MP-FRAP

As shown in Figs. 3 and 5, the standard model yields accurate values for the diffusion coefficient at negligible flows in both simulations and experiments. As velocities become appreciable and increase the rate of recovery, the standard model compensates by erroneously raising the diffusion coefficient in the resultant fit. At extremely high flow velocities, this error is obvious to the experimentalist as the shape of the recovery curve changes dramatically and

the standard model fit becomes visibly poor (Fig. 8a). However, in the regime where velocity only moderately influences the recovery, the shape change is subtle and the standard model may still yield a good looking fit while offering an inaccurate diffusion coefficient (Fig. 8b). Herein lies the danger when the standard model is applied to an unfamiliar system with modest convective flows. This effect can be quantified with our experimentally derived cutoff scaled velocity of  $v_s \approx 0.3$ . For scaled velocities greater than this, at typical S/N values, fitting with the standard MP-FRAP model will give erroneous values of  $D$ .

## Flow MP-FRAP

The flow MP-FRAP model offers a significant improvement over the standard model by yielding accurate diffusion coefficients in the presence of significant flows that generate errors in the standard model. The flow model is also capable of accurately determining the flow velocity. However, the simulations show that when either diffusion or velocity dominates the fluorescence recovery, the flow model poorly determines the non-dominant parameter, thus setting up three regimes: 1. diffusion-dominated, in which only the diffusion coefficient is accurately determined; 2. balanced, in which both diffusion and velocity are accurately determined; and 3. velocity-dominated, in which only velocity is accurately determined. By defining a scaled velocity parameter,  $v_s = v(\omega_r/8D)$ , simulations reveal that each of the two transitions between the regimes occur over the same range of scaled velocities for all magnitudes of diffusion coefficients. These transitions will shift slightly when fluorescence recoveries with differing amounts of noise and/or bleach depths are analyzed, such that the balanced regime is broadest with low noise and/or high bleach depth and is narrowest with high noise and/or low bleach depth.

As a direct experimental measure of the abilities of the flow model, we conducted MP-FRAP in a simple system with known flow, using a fluorescent dye conjugated to a macromolecule (BSA or dextran) with a known diffusion rate. In agreement with the simulations, a comparison of fits to the standard and flow models showed that the flow model yields accurate diffusion coefficients for velocities approximately ten times as large as the maximum velocity at which the standard model was able to yield an accurate diffusion coefficient. Also as expected, when velocities were appreciable yet small, the flow model accurately determined the diffusion coefficient, but poorly determined the velocity. Specifically, for typical experimental noise ( $\sim 4\%$ ) and bleach depth ( $\sim 0.5$ ), the cutoff velocity for transition from diffusion-dominated to balanced recovery was  $v_s \approx 0.2$ , while the cutoff velocity for transition from balanced recovery to flow-dominated was  $v_s \approx 3$ . For both transitions, the standard deviation of the measured value of the non-dominant parameter was a more sensitive indicator of problems with the fit than was the actual average value of the non-dominant parameter.

## *In vivo* application

As an illustrative demonstration of the flow model *in vivo*, we chose to measure diffusion and convection within tumor blood vessels. The RBC velocity provided a separate indicator of convective flow and allowed us to evaluate our model. Our first example was a vessel with extremely slow RBC velocity, and hence a low scaled velocity of 0.08 (based upon literature values of  $D$  extrapolated to plasma at  $37^\circ\text{C}$ ). From this we predicted that accurate values for



the diffusion coefficient would be produced by both the standard model and the flow model, but an inaccurate value for the measured velocity would be given by the flow model, due to the dominance of diffusion over flow. Our second example was a vessel with a scaled velocity of 0.45, in between the two cutoff velocities, suggesting that the standard model would be unable to produce an accurate value of  $D$ , while the flow model would accurately determine both  $D$  and  $v$ . Our third example was a vessel with a scaled velocity of 6.24, above the highest cutoff velocity, predicting inaccurate values of  $D$  from both models, but an accurate velocity measurement from the flow model. In each case, the *in vivo* data performed as predicted. This demonstrates *in vivo* that the flow model extends the range of flow velocities over which accurate diffusion coefficients can be determined by an order of magnitude, and that the flow model can also determine the flow velocity accurately over a wide range of flows.

## Future Applications

In future experiments in which both  $D$  and  $v$  are not known *a priori*, the flow model can be used for fitting the MP-FRAP curves and the typical cutoff velocities determined here can act as a retrospective “sanity check.” If the output  $v$  and  $D$  are within the cutoff velocities, one can assume the values are correct. This is because at no point does the absolute error in the non-dominant parameter grow large enough to map the incorrect output parameters into the “balanced” regime. For example, the MP-FRAP simulations that produced the data on the extreme right hand side of Fig. 3 were performed at a scaled velocity of 300 and produced an output  $D$  ratio of 10 and an output  $v$  ratio of 1. The output scaled velocity is hence (incorrectly) determined to be 30. This is erroneously low, but still above the cutoff velocity, and hence would be easily rejected by the experimentalist as indicating incorrect values of the fit parameters, even if the fit appears reasonable.

## Conclusion

In this paper we derived an improved model of multiphoton fluorescence recovery after photobleaching which explicitly accounts for the presence of convective flow as well as diffusion. Using simulations and *in vitro* experiments, we demonstrated that this extends the ability of MP-FRAP to determine diffusion coefficients accurately in the presence of flow to flow velocities an order of magnitude higher than are possible with the standard model of MP-FRAP, which does not account for flow. We also determined experimentally useful “cutoff velocities” which, for typical experimental parameters, predict the range of scaled velocities over which the flow model allows MP-FRAP to produce accurate diffusion coefficients, as well as accurate flow velocities.

## Appendix

The time-dependent concentration of unbleached fluorophore immediately after the termination of a bleach pulse is given by Brown et. al (13). When converted to Cartesian coordinates this is given by:

$$c(x, y, z; t) = \sum_{n=0}^{\infty} A_n(t) e^{-\mu_n(t)x^2} e^{-\mu_n(t)y^2} e^{-\nu_n(t)z^2} \quad (\text{A1})$$

where,

$$A_n(t) = c_o \frac{(-\beta)^n}{n!} \frac{1}{(1 + 8bnDt/w_z^2)^{1/2} (1 + 8bnDt/w_r^2)} \quad (\text{A2a})$$

$$\mu_n(t) = \frac{2bn}{w_r^2} \frac{1}{(1 + 8bnDt/w_r^2)} \quad (\text{A2b})$$

$$\nu_n(t) = \frac{2bn}{w_z^2} \frac{1}{(1 + 8bnDt/w_z^2)} \quad (\text{A2c})$$

An attenuated laser beam is used to monitor the changing concentration profile. The fluorescence recovery is given by (13):

$$F(t) = \frac{\delta_m E}{m} \int \langle I_{mo}^m(x, y, z) \rangle c(x, y, z; t) 2\pi r dr dz \quad (\text{A3})$$

where  $\delta_m$  is the multiphoton fluorescence action cross-section,  $\langle I_{mo}^m(x, y, z) \rangle$  is the time average of the bleach intensity raised to the  $m$ th power, and  $m$  is the number of photons required to produce fluorescence from a single fluorophore.

We first consider flow along the x-axis. To solve for  $F(t)$  in this case we choose a frame of reference in which we have a source moving along the x-direction (the concentration distribution moving under flow) and a stationary observer (the focal volume monitoring the intensity). In the frame of reference of the observer,  $x' = x + vt$ ,  $y' = y$ , and  $z' = z$ . The time-dependent fluorophore concentration is now:

$$c(x, y, z; t) = \sum_{n=0}^{\infty} A_n(t) e^{-\mu_n(t)(x'-vt)^2} e^{-\mu_n(t)y'^2} e^{-\nu_n(t)z'^2} \quad (\text{A4})$$

The expression for the monitoring intensity distribution does not change from the case of both source and observer stationary (13):

$$\langle I_{mo}^m(x', y', z') \rangle = \langle I_o \rangle e^{(2m/w_r^2)x'^2} e^{(2m/w_r^2)y'^2} e^{(2m/w_z^2)z'^2} \quad (\text{A5})$$

Substituting Eqs. A4 and A5 into Eq. A3 yields:

$$F(t) = \frac{\delta_m E}{m} \langle I_o \rangle \sum_{n=0}^{\infty} A_n(t) \int_{-\infty}^{+\infty} e^{-(\mu_n(t) + 2m/w_r^2)(x'-vt)^2} dx' \\ \times \int_{-\infty}^{+\infty} e^{-(\mu_n(t) + 2m/w_r^2)y'^2} dy' \int_{-\infty}^{+\infty} e^{-(\mu_n(t) + 2m/w_r^2)z'^2} dz' \quad (\text{A6})$$

Before integrating, we first rewrite the exponential in  $x'$  by expanding the exponent, completing the square in  $x'$ , then making the variable substitution:

$$\gamma' = x' - \frac{\mu_n(t)vt}{\mu_n(t) + 2m/w_r^2} \quad (\text{A7})$$

The expression for the fluorescence recovery now looks like:

$$F(t) = \frac{\delta_m E}{m} \langle I_o \rangle \sum_{n=0}^{\infty} \bar{A}_n(t) \int_{-\infty}^{+\infty} e^{-(\mu_n(t)+2m/w_r^2)\gamma'^2} d\gamma' \\ \times \int_{-\infty}^{+\infty} e^{-(\mu_n(t)+2m/w_r^2)y'^2} dy' \int_{-\infty}^{+\infty} e^{-(\mu_n(t)+2m/w_r^2)z'^2} dz' \quad (\text{A8})$$

where,

$$\bar{A}_n(t) = A_n(t) \exp \left[ -\frac{2m\mu_n(t)v^2 t^2}{2m + \mu_n(t)w_r^2} \right] \quad (\text{A9})$$

The integrals in Eq. A8 are now all first order Gaussians. When the integrals are complete and  $\bar{A}_n(t)$ ,  $\mu_n(t)$ , and  $\nu_n(t)$  have been substituted in, the simplified expression, letting  $m = b = 2$  for a two-photon process, is:

$$F(t) = F_o \sum_{n=0}^{\infty} \frac{(-\beta)^n}{n!} \frac{\exp \left[ -\frac{4n(vt/w_r)^2}{1+n+16nDt/w_r^2} \right]}{(1+n+16nDt/w_r^2)(1+n+16nDt/w_z^2)^{1/2}} \quad (\text{A10})$$

We may also express the equation in terms of system-specific variables,  $\tau_D = w_r^2/8D$  and  $\tau_v = w_r/v$ :

$$F(t) = F_o \sum_{n=0}^{\infty} \frac{(-\beta)^n}{n!} \frac{\exp \left[ -\frac{4n(t/\tau_v)^2}{1+n+2nt/\tau_D} \right]}{(1+n+2nt/\tau_D)(1+n+2nt/R\tau_D)^{1/2}} \quad (\text{A11})$$

Finally, this equation can be generalized to flow with a component along all three axes ( $v^2 = v_x^2 + v_y^2 + v_z^2$ ) as follows:

$$F(t) = F_o \sum_{n=0}^{\infty} \frac{(-\beta)^n}{n!} \frac{\exp \left[ -\frac{4n[t^2/(\tau_{v_x}^2 + \tau_{v_y}^2) + t^2/\tau_{v_z}^2]}{1+n+2nt/\tau_D} \right]}{(1+n+2nt/\tau_D)(1+n+2nt/R\tau_D)^{1/2}} \quad (\text{A12})$$

where,  $\tau_{v_x} = w_r/v_x$ ,  $\tau_{v_y} = w_r/v_y$ , and  $\tau_{v_z} = w_z/v_z$ .

## Acknowledgements

This work was funded by a Department of Defense Era of Hope Scholar Award (W81XWH-05-1-0396) and a Pew Scholar in the Biomedical Sciences Award to E.B. Special thanks to Ryan Burke for overseeing all cell and tissue culture, and to Khawarl Liverpool for his careful dorsal skinfold chamber surgeries.

## References

1. Peters, R., J. Peters, K. Tews, and W. Bahr. 1974. Microfluorimetric study of translational diffusion of proteins in erythrocyte membranes. *Biochim Biophys Acta*. 367:282–294.
2. Axelrod, D., D. E. Koppel, J. Schlessinger, E. Elson, and W. W. Webb. 1976. Mobility Measurement by Analysis of Fluorescence Photobleaching Recovery Kinetics. *Biophys J*. 16:1055–1069.
3. Eididin, M., M. Zagjansky, and T. Lardner. 1976. Measurement of membrane protein lateral diffusion in single cells. *Science*. 191:466–468.
4. Schlessinger, J., D. E. Koppel, D. Axelrod, K. Jacobson, W. W. Webb, and E. Elson. 1976. Lateral transport on cell membranes: mobility of concanavalin A receptors on myoblasts. *PNAS*. 73:2409–2413.
5. Berk, D. A., F. Yuan, M. Leunig, and R. K. Jain. 1993. Fluorescence Photobleaching with Spatial Fourier Analysis: Measurement of Diffusion in Light-Scattering Media. *Biophys J*. 65:2428–2436.
6. Denk, W., J. H. Strickler, and W. W. Webb. 1990. Two-Photon Laser Scanning Fluorescence Microscopy. *Science*. 248:73–76.
7. Brown, E. B., R. B. Campbell, Y. Tsuzuki, L. Xu, P. Carmeliet, D. Fukumura, and R. K. Jain. 2001. *In vivo* measurement of gene expression, angiogenesis, and physiological function in tumors using multi-photon laser scanning microscopy. *Nature Medicine*. 7:864–868.
8. Jain, R. K., R. J. Stock, S. R. Chary, and M. Rueter. 1990. Convection and diffusion measurements using fluorescence recovery after photobleaching and video calibration. *Microvasc Res*. 39:77–93.
9. Berland, K. M., P. T. C. So, and E. Gratton. 1995. Two-photon fluorescence correlation spectroscopy: method and application to the intracellular environment. *Biophys J*. 68:694–701.
10. Mertz, J., C. Xu, and W. W. Webb. 1995. Single-molecule detection by two-photon excited fluorescence. *Opt Lett*. 20:2532–2534.
11. Wiseman, P. W., J. A. Squier, M. H. Ellisman, and K. R. Wilson. 2000. Two photon image correlation spectroscopy and image cross-correlation spectroscopy. *J Microsc*. 200:14–25.
12. Kolin, D. L., D. Ronis, and P. W. Wiseman. 2006. k-space image correlation spectroscopy: a method for accurate transport measurements independent of fluorophore photophysics. *Biophys J*. 91:3061–3075.

13. Brown, E. B., E. S. Wu, W. Zipfel, and W. W. Webb. 1999. Measurement of Molecular Diffusion in Solution by Multiphoton Fluorescence Photobleaching Recovery. *Biophys J.* 77:2837–2849.
14. Kleinfeld, D., P. P. Mitra, F. Helmchen, and W. Denk. Fluctuations and stimulus-induced changes in blood flow observed in individual capillaries in layers 2 through 6 of rat neocortex. *Proc Natl Acad Sci USA.*
15. Leunig, M., F. Yuan, M. D. Menger, Y. Boucher, A. E. Goetz, K. Messmer, and R. K. Jain. 1992. Angiogenesis, Microvascular Architecture, Microhemodynamics, and Interstitial Fluid Pressure Density During Early Growth in Human Adenocarcinoma LS 174T in SCID mice. *Cancer Res.* 52:6553–6560.
16. Lanni, F., D. L. Taylor, and B. R. Ware. 1981. Fluorescence Photobleaching Recovery in Solutions of Labeled Actin. *Biophys J.* 35:351–364.
17. Fuh, C. B., S. Levin, and J. C. Giddings. 1993. Rapid Diffusion Coefficient Measurements Using Analytical SPLITT Fractionation: Application to Proteins. *Anal Biochem.* 208:80–87.
18. Pluen, A., P. A. Netti, R. K. Jain, and D. A. Berk. 1999. Diffusion of Macromolecules in Agarose Gels: Comparison of Linear and Globular Configurations. *Biophys J.* 77:542–552.
19. Chary, S. R., and R. K. Jain. 1989. Direct measurement of interstitial convection and diffusion of albumin in normal and neoplastic tissues by fluorescence photobleaching. *Proc Natl Acad Sci USA.* 86:5385–5389.
20. Pluen, A., Y. Boucher, S. Ramanujan, T. D. McKee, T. Gohongi, E. di Tomaso, E. B. Brown, Y. Izumi, R. B. Campbell, D. A. Berk, and R. K. Jain. 2001. Role of tumor-host interactions in interstitial diffusion of macromolecules: cranial vs. subcutaneous tumors. *Proc Natl Acad Sci USA.* 98:4628–4633.
21. Jain, R. K. 1988. Determinants of tumor blood flow: a review. *Cancer Res.* 48:2641–2658.

**Table 1** Results of fitting experimental *in vivo* data of diffusion and convection in tumor vessels using both the standard and flow models.

	$v_s$	$D_{\text{standard}} (\mu\text{m}^2/\text{s})$	$D_{\text{flow}} (\mu\text{m}^2/\text{s})$	$v_{\text{flow}} (\mu\text{m}/\text{s})$	$v_{\text{RBC}} (\mu\text{m}/\text{s})$
vessel 1	$0.08 \pm 0.02$	9.28	9.28	0.02	$14 \pm 3$
vessel 2	$0.45 \pm 0.05$	19.6	9.68	69.3	$83 \pm 10$
vessel 3	$6.24 \pm 0.44$	250	34.9	987	$1139 \pm 80$

## Figure Legends

### Figure 1.

Comparison of the recovery of simulated MP-FRAP curves for a macromolecule with  $D = 9\mu\text{m}^2/\text{s}$  with differing values of flow velocity. The red curve is a diffusion-only recovery ( $v = 0\mu\text{m}/\text{s}$ ), while the blue recovery curve has a moderate amount of flow ( $v = 120\mu\text{m}/\text{s}$ ), and the green recovery curve is velocity dominated ( $v = 500\mu\text{m}/\text{s}$ ). The shape of the curve changes as flow increases, eventually leading to an almost sigmoidal shape for velocity-dominated recoveries.

### Figure 2.

Equipment diagram for FRAP apparatus used for both *in vitro* and *in vivo* studies. To obtain line scan images for velocity comparison, a laser scanning system was included in the system. An additional dichroic mirror and PMT were also included to separate and measure the red fluorescence of the polystyrene beads.

### Figure 3.

Simulated fluorescence recovery curves were generated with the flow model, keeping the bleach depth parameter and noise level constant at 0.6 and 3%, respectively, while exploring a range of velocities for each of a set of diffusion coefficients (from left to right:  $D = 0.5, 1, 5, 10, 50, 100, 500 \mu\text{m}^2/\text{s}$ ). The data was fit to the standard MP-FRAP model, and the diffusion coefficient produced by the fit was normalized to the input diffusion coefficient. Hence, an accurate result produces a ratio of one. As the input velocity increases beyond a certain cutoff value, the standard model yields a growing overestimate to the diffusion coefficient. By scaling the input velocity along the horizontal axis (inset), the curves for each value of the diffusion coefficient collapse onto a single curve.

### Figure 4.

Simulated fluorescence recovery curves were generated with the flow model, keeping the input bleach depth parameter and noise level constant while exploring a range of velocities for each of two diffusion coefficients representing FITC-BSA and FITC-2000kD dextran. The data was fit to the flow model, and the diffusion coefficient or flow velocity produced by the fit was normalized to the input value. Hence, an accurate result produces a ratio of one. In the case that either diffusion or velocity dominates the fluorescence recovery, the fit accurately determines the dominant parameter, while poorly determining the non-dominant parameter. For a wide range of balanced recoveries, both diffusion and velocity are well-determined. In (a),  $\beta = 0.6$  and  $S/N = 3\%$ , experimentally representative values. Arrows point to regimes where the standard deviations in the non-dominant parameter are high, even though the average value remains close to one. In (b),  $\beta = 0.6$  and  $S/N = 10\%$ ; the increase in noise leads to a more rapid rise in the diffusion coefficient in the velocity-dominated regime. In (c),  $\beta = 1.0$  and  $S/N = 3\%$ ; the deeper bleach depth reduces the standard deviations, especially in the diffusion coefficient in the velocity-dominated regime.

**Figure 5.**

A series of experimental fluorescence recovery curves for FITC-BSA and FITC-2000kD dextran were taken over a wide range of known flow velocities. The curves were then fit to both the standard MP-FRAP model and the flow MP-FRAP model, and the diffusion coefficient produced by the fit was normalized to the input value. Hence, an accurate result produces a ratio of one. The diffusion coefficients taken from the respective flow model fits are presented here as ratios with respect to the diffusion coefficient measured in a system without flow and fit to the standard model. As the flow velocity grows beyond  $v_s \approx 0.3$ , the standard MP-FRAP model yields an increasing overestimate to the diffusion coefficient. The improved flow model, however, continues to provide accurate diffusion coefficients for scaled velocities up to  $v_s \approx 3$ , approximately ten times larger than the cutoff velocity for the standard model.

**Figure 6.**

A series of experimental fluorescence recovery curves for FITC-BSA and FITC-2000kD dextran were taken over a wide range of known flow velocities. The diffusion coefficients taken from the respective fits to the flow model are presented here as ratios with respect to the diffusion coefficient measured in a system without flow and fit to the standard model. An accurate result produces a ratio of one. Dotted lines delineate the two experimentally determined cutoff velocities which define a parameter space in which the flow model accurately determines one (or both) parameters. The velocities taken from the respective fits are presented as ratios with respect to velocities measured via line-scans. As with the simulations, in the case that either diffusion or velocity dominates the fluorescence recovery, the fit correctly determines the dominant parameter, while poorly determining the non-dominant parameter. A wide range of balanced recoveries,  $0.2 \lesssim v_s \lesssim 3$ , yields accurate fits for both parameters.

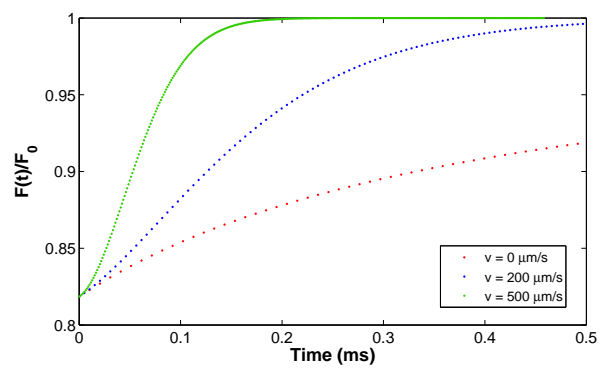
**Figure 7.**

Experimental fluorescence recovery curves of FITC-dextran, flowing in vessels of 4T1 tumors implanted in the dorsal region of male Balb/cByJ mice. Each curve represents a different fitting regime for the flow model: (a) diffusion dominated recovery, only diffusion is accurately determined; (b) balanced recovery, both diffusion and flow velocity are accurately determined; (c) velocity dominated, only velocity is accurately determined.

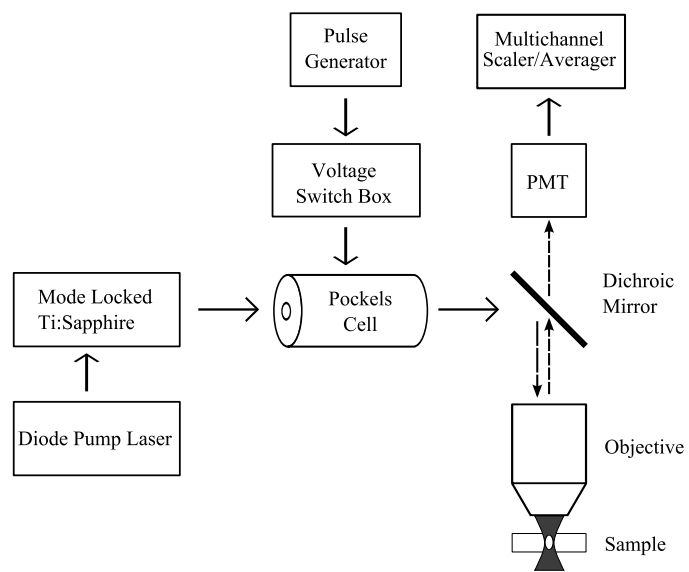
**Figure 8.**

Simulated fluorescence recovery curves, generated with the flow model and fit to the standard model. In (a) the recovery is velocity-dominated and there is an obvious alteration in the shape of the recovery curve, which is visibly poorly fit by the standard model. In (b) the recovery is balanced under the influences of diffusion and velocity. Although the fit looks good by eye, the standard model produces a diffusion coefficient 25% larger than the input value.

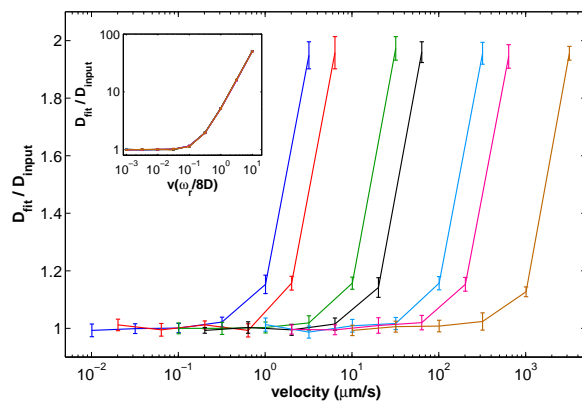




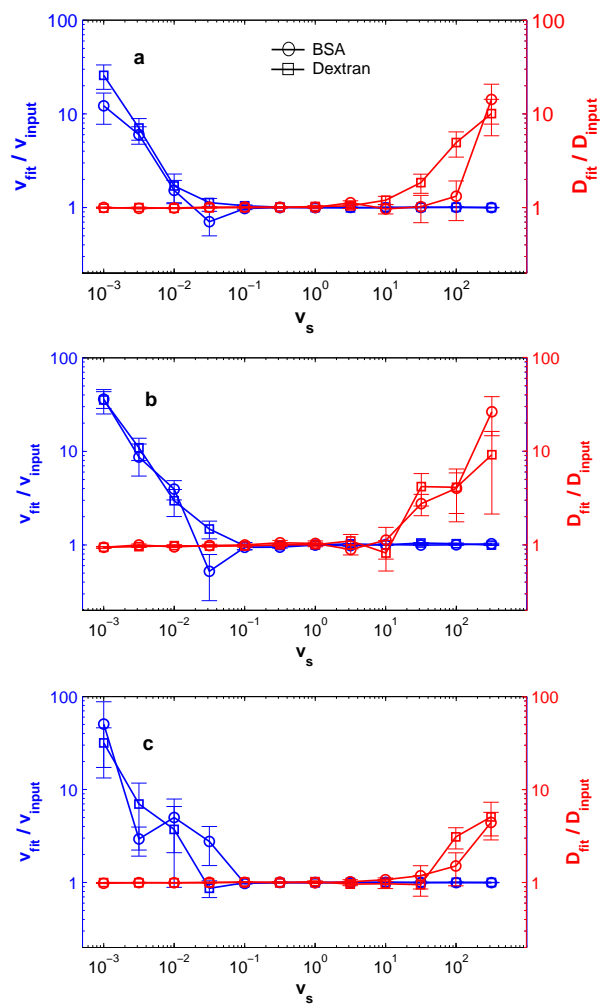
Sullivan\_figure 1



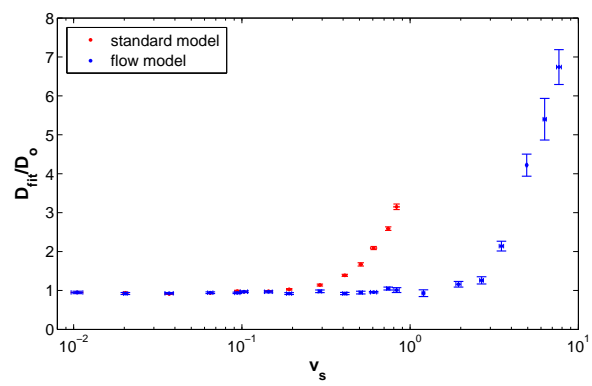
Sullivan figure 2



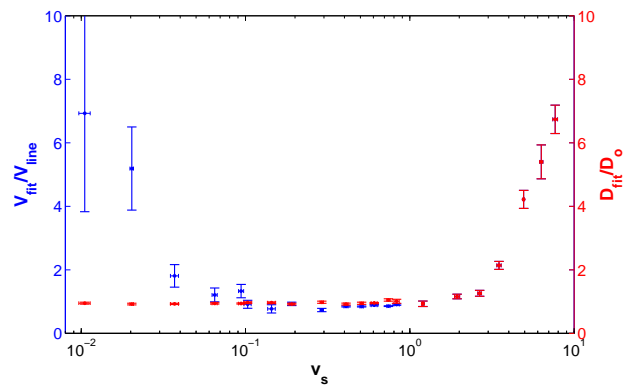
Sullivan\_figure 3



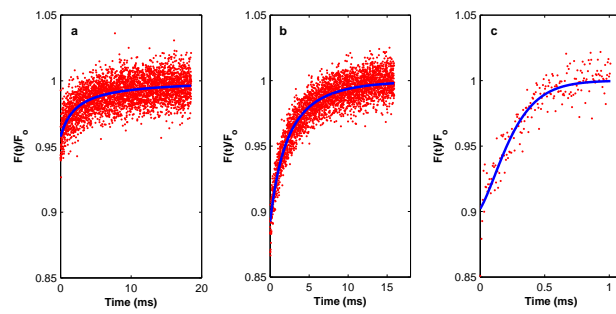
Sullivan\_figure 4



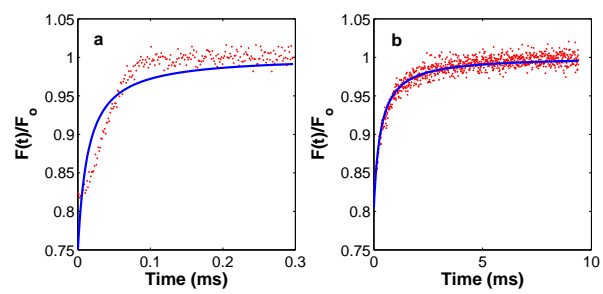
Sullivan\_figure 5



Sullivan\_figure 6



Sullivan\_figure 7



Sullivan\_figure 8